Processes Controlling Precipitation in Shallow, Orographic, Trade Wind Convection

CAMPBELL D. WATSON,* RONALD B. SMITH, AND ALISON D. NUGENT

Department of Geology and Geophysics, Yale University, New Haven, Connecticut

(Manuscript received 12 November 2014, in final form 11 March 2015)

ABSTRACT

A sharp reduction in precipitation was observed on the island of Dominica in the Caribbean during a 2011 field campaign when the trade winds weakened and convection transitioned from mechanically to thermally driven. The authors propose four hypotheses for this reduction, which relate to (i) the triggering mechanism, (ii) dry-air entrainment, (iii) giant sea-salt aerosol, and (iv) small-island-derived aerosol. The plausibility of the first three hypotheses is the focus of this study.

Aircraft observations show the dynamics of the orographic cumulus clouds at flight level are surprisingly similar, irrespective of how they are triggered. However, the orographic cumulus clouds are consistently shallower when the trade winds are weak, which the authors attribute to a drier and shallower cloud layer compared to days with stronger trade winds. The strong negative influence of dry-air entrainment in a drier environment on cumulus depth and liquid water content is qualitatively demonstrated using an entraining plume model and the WRF Model. Although the models appear more sensitive than observations to entrainment and cloud size, the sensitivity tests have some resemblance to observations. The authors also find evidence of sea-salt aerosol entering the base of marine cumulus on strong wind days using an aircraft-mounted lidar and other instruments. Although each hypothesis is plausible, the complex interplay of these processes makes determining the controlling mechanisms difficult. Ultimately, the authors' analysis rejects the hypothesis (i) triggering, while supporting (ii) entrainment and (iii) sea-salt aerosol.

1. Introduction

While many types of continental and maritime cumulus and stratocumulus clouds have been studied, the simplest and most repetitive clouds are orographic cumulus. Depending on the strength of the low-level flow, orographic cumulus clouds are triggered repeatedly over the terrain by surface heating (thermally driven) or the forced ascent of conditionally unstable flow (mechanically driven). The present study is concerned with the shallow, orographic cumulus clouds that form over Dominica—a small and mountainous island in the eastern Caribbean. In undisturbed conditions, the cloud fraction is substantially higher and the cumulus more closely packed than over the open ocean, illustrated by the *Landsat-8* image in Fig. 1 (on this day the trades were strong and convection likely mechanically driven). Time-lapse images looking upstream of the island show the initiation of new and invigoration of pre-existing cumuli over the windward slopes, creating a pronounced orographic enhancement of 3–5 times the overocean precipitation (Smith et al. 2009).

Dominica was the subject of a 2011 field campaign called the Dominica Experiment (DOMEX; Smith et al. 2012). The field campaign observed both weak and strong wind conditions, revealing a very high sensitivity of the usually heavy, convective orographic precipitation to trade wind speed (see Fig. 4 in Smith et al. 2012). When the trades were weak ($<5\,\mathrm{m\,s^{-1}}$) and convection thermally driven, the heavy downpours abated and two off-island radars showed a pronounced reduction in over-island precipitation. This is consistent with the absence of a diurnal signature in over-island precipitation (Smith et al. 2009). However, a physical explanation for the negligible orographic precipitation enhancement during weak wind conditions remains elusive.

The orographic flow dynamics and bulk microphysical properties of the orographic cumulus clouds over

* Current affiliation: IBM T. J. Watson Research Center, Yorktown Heights, New York.

Corresponding author address: Campbell D. Watson, Department of Geology and Geophysics, Yale University, 210 Whitney Ave., New Haven, CT 06511.
E-mail: campbell.watson@yale.edu

DOI: 10.1175/JAS-D-14-0333.1

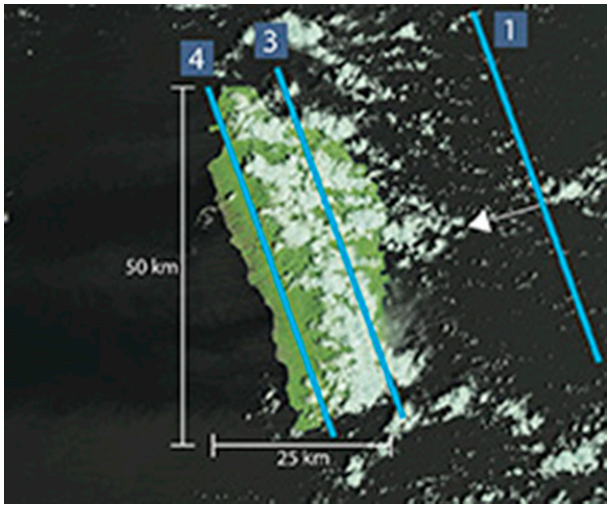

FIG. 1. Cloud structure on 6 Apr 2014 (a typical "high wind day") captured by the operational land imager on board the *Landsat-8*. The white arrow shows the typical trade wind direction. The blue lines show the approximate location of flight legs 1, 3, and 4. (Note: only the over-island segment of legs 3 and 4 are shown in this figure.)

Dominica have been studied by Smith et al. (2009, 2012), Kirshbaum and Smith (2009), Minder et al. (2013), Nugent et al. (2014), Russotto et al. (2013), and Nugent and Smith (2014). Previous studies of trade wind cumulus also help define the upstream conditions, including observational field campaigns [e.g., Atlantic Tradewind Experiment (ATEX), Barbados Aerosol Cloud Experiment (BACEX), Barbados Oceanographic and Meteorological Experiment (BOMEX), Rain in (shallow) Cumulus over the Ocean (RICO)], modeling studies (e.g., Siebesma et al. 2003; Zhao and Austin 2005; Abel and Shipway 2007; Heus and Jonker 2008; Jensen and Lee 2008; Nuijens and Stevens 2012; Nie and Kuang 2012), and theoretical studies (e.g., Arakawa and Schubert 1974; Betts and Ridgway 1989; Stevens and Brenguier 2009). From these prior studies, we propose the following four hypotheses for what controls the high sensitivity of precipitation to trade wind speed on Dominica: (i) The dynamics of the orographic cumulus triggered by thermally driven convection differ in some important way(s) to those triggered by mechanically driven convection. (ii) The drier and shallower cloud-layer environment on weak wind days reduces the depth of the cumulus clouds above Dominica and, thereby, the cloud-top liquid water content (LWC). (iii) The weaker trade winds reduce the concentration of giant sea-salt aerosol generated by wind speed–dependent wave breaking, delaying the onset of the coalescence process over the island. (iv) Under weak winds, the addition of small, island-derived aerosol lofted by the surface-based, thermally driven convection increases the cloud droplet number density and reduces the mean droplet diameter, suppressing the formation of raindrop nuclei.

In this study, we investigate the plausibility of the first three hypotheses using aircraft observations from DOMEX and conventional analysis tools. We do not intend to prove that any of these hypotheses are the controlling factor; rather, we search for insight into their potential importance to the observed precipitation sensitivity. Evidence in support of the fourth hypothesis has been presented in Smith et al. (2012) and Nugent et al. (2014).

The manuscript is structured as follows. Section 2 describes the DOMEX field campaign and observational dataset used in this study. Section 3 presents characteristics of the orographic clouds and convection in three different wind speed conditions. Section 4 examines the upstream thermodynamic structure for each of the research flights, which helps define the environmental profiles used in two sets of idealized model simulations. Finally, section 5 presents evidence of sea-salt aerosol in the marine boundary layer entering cloud base on strong wind days. A summary of these results is presented in section 6.

2. The observational dataset

The DOMEX field campaign included 21 research flights (RFs) with the Wyoming King Air research aircraft over and around the island of Dominica. Measurements from seven research flights are used: RF7, RF8, RF11, RF12, RF13, RF17, and RF18. (The other 14 research flights were excluded because of large-scale cloudiness, an incomplete flight plan, and/or nonfunctioning or malfunctioning instruments.) Each research flight began with an upwind profile (from 4 km to 150 m) followed by six horizontal legs (see Fig. 3 in Smith et al. 2012). We only use measurements from the upwind profile and legs 1, 3, and 4 (Fig. 1). Leg 1 was designed to measure the ambient trade wind environment around 20 km upwind of Dominica. It was flown at two altitudes: 370 m and 1.3 km, called leg 1L and 1H, respectively. The lowest clouds typically formed at 600–700 m, hence leg 1L measured the subcloud marine boundary layer and leg 1H measured the cloud layer. Legs 3 and 4 were designed to measure the above-island convection, flown at 1.7 km. The start and end of the leg 3 and 4 flight tracks were over the open ocean, whereas the central segment of these flight tracks was over the island. In this study, we use only the above-island measurements.

The aircraft had multiple instruments to measure the flight-level winds, thermodynamics, cloud and rain particles, and aerosols. These quantities were measured at 1, 10, and 25 Hz; an average airspeed of 90 m s^{-1} gives a sampling distance of 90, 9, and 4 m, respectively. The

TABLE 1. Leg-average flow parameters, cloud properties, and environmental characteristics for the low, medium, and high wind cases. All quantities were measured by the aircraft, except for rainfall, which was measured at the Freshwater Lake mountain weather station. The bold numbers indicate distinctly larger values than numbers in other wind speed categories. For context, flight legs within the vicinity of convection above the island are legs 3 and 4 on low wind days and leg 3 on medium and high wind days.

Properties	Units	Instruments	Leg	RF7, -8 (low)	RF11, -18 (medium)	RF12, -13, -17 (high)
		Over-island measurements, $z = 1.8$ km				
Daily rainfall	mm day^{-1}	Mountain weather station	N/A	0.1	**7.8–37.9**	**11.4–36.3**
Cloudiness fraction	%	CDP	3	15	9	**20**
			4	**27**	5	3
Cloud-top height	km	WCR	3	2.7	2.5	**3.3**
			4	2.8	2.5	2.0
Radar reflectivity above flight level	dBZ ($\times 10 \log_{10}$)	WCR	3	−20	−12	**−5**
			4	−25	−15	**−9**
Mixing ratio	g kg^{-1}	Licor	3	10.3	10.6	11.6
			4	10.0	11.0	11.2
Out-of-cloud aerosol concentration	cm^{-3}	PCASP	3	**310**	45	45
			4	**360**	40	35
Updraft/downdraft fraction ($w' > 1$ m s^{-1}/$w' < -1$ m s^{-1})	%	Gust probe	3	10.3/11.1	3.8/4.1	9.6/11.6
			4	**16.6/19.3**	7.5/7.3	22.0/22.0
Total/average number of cloud cores		CDP, gust probe	3	36/6.0	15/3.8	**46/7.7**
			4	**62/10.3**	6/1.5	9/1.5
Number of narrow/intermediate/ wide cloud cores		CDP, gust probe	3	5.2/0.8/0.0	3.5/0.2/0.0	**5.5/1.8/0.4**
			4	**7.8/1.5/1.0**	0.7/0.7/0.0	0.8/0.5/0.1
Cloud droplet number concentration (average per cloud core)	cm^{-3}	CDP	3	**203**	115	106
			4	**450**	112	115
Cloud droplet MVD (average per cloud core)	μm	CDP	3	17.7	**24.2**	**24.9**
			4	15.3	21.9	23.9
		Upwind measurements, $z = 300$ m (1L), $z = 1.2$ km (1H)				
Wind speed	m s^{-1}	Gust probe	1L	2.9	6.6–7.0	9.1–11.4
Cloudiness fraction	%	CDP	1H	0.1	0.3	**6.0**
Lifting condensation level (derived)	m	Various	1L	750	731	714
Cloud base	m	Lidar	1L	760	694	752
Mixing ratio	g kg^{-1}	Licor	1L	15.3	16.5	16.4
			1H	9.5	**11.4**	**12.3**
Out-of-cloud aerosol concentration	cm^{-3}	PCASP	1H	**125**	60	66
Aerosol concentration (radius: $>0.5\,\mu$m)	cm^{-3}	PCASP	1L	0.006	0.026	**0.042**
CDP droplet concentration (radius: 1–5 μm)	cm^{-3}	CDP	1L	0.008	0.046	**0.076**

aircraft also carried the Wyoming cloud radar ($\lambda = 3160\,\mu$m) and the Wyoming cloud lidar ($\lambda = 0.355\,\mu$m; Wang et al. 2009).

Five instruments on board the aircraft were capable of measuring the cloud LWC. After exhaustive analysis with DOMEX lead project manager, Jeffrey French (2013, personal communication), the DMT cloud droplet probe (CDP; $\lambda = 0.658\,\mu$m; Lance et al. 2010) was selected as the primary cloud microphysics measurement for this study because it does not suffer from the splashing of precipitation-sized droplets (an important consideration in precipitating cumulus) and remained robust for the duration of the campaign. The CDP is a cloud particle spectrometer that measures droplets at 10 Hz with radius 1–25 μm in concentrations as high as 2000 cm^{-3}.

Air temperature was measured by a reverse flow thermometer. Although the instrument was designed to reduce the effects of wetting, the high LWCs, nonuniform cloud structure and updrafts exceeding 5 m s^{-1} can cause significant in-cloud temperature errors. While corrections can be applied (e.g., Eastin et al. 2002; Wang and Geerts 2009), we have chosen to use temperature measurements sparingly in this study.

Finally, as in Smith et al. (2012), each research flight is grouped according to its ambient trade wind speed (u-amb), estimated from the average wind speed perpendicular to Dominica along leg 1L. The low wind class (u-amb < 5 m s^{-1}) includes RF7 and RF8, the medium wind class (u-amb = 5 to 8 m s^{-1}) includes RF11 and RF18, and the high wind class (u-amb > 8 m s^{-1}) includes

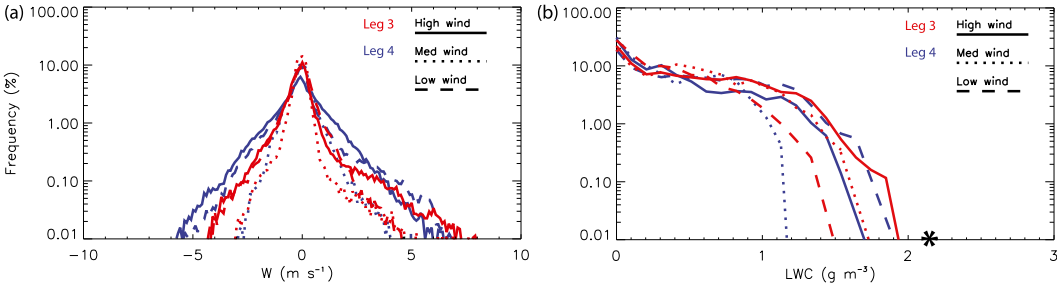

FIG. 2. Frequency distribution of (a) vertical velocity (w') and (b) in-cloud LWC measurements on low, medium, and high wind days along legs 3 and 4. The velocity w' is the perturbation from the leg mean, which negates the layer-lift effect. The asterisk in (b) indicates the predicted adiabatic LWC of 2.1 g m^{-3} from subcloud measurements along leg 1L.

RF12, RF13, and RF17. Table 1 presents a range of statistics for each of the wind speed classes from aircraft measurements upwind of and over the island. To refer to the wind speed class and associated flight leg number, we also use the notation LOW-3, LOW-4, MED-3, etc.

3. Clouds and convection over Dominica

a. General characteristics

Smith et al. (2012) identified two regimes of convective triggering from DOMEX observations. When the trade winds were weak (low wind days, RF7, RF8), convection was thermally driven by surface heating. Each research flight occurred in the early afternoon when diurnal–thermal convection was fully established. Aircraft measurements suggest clouds and convection were concentrated above the downwind slope: LOW-4 had a higher cloudiness fraction (ratio of in-cloud to out-of-cloud CDP measurements), stronger updrafts, and higher LWCs compared to LOW-3 (Table 1 and Fig. 2). Cloud radar echoes are consistent with this picture (e.g., Figs. 3a,b), revealing more evenly spaced cumulus clouds along LOW-4 and an average cloud-top height[1] of 2.7 km along LOW-3 and 2.8 km along LOW-4.

When the trade winds strengthened (medium and high wind days), thermal convection was suppressed by ventilation and cloud shading, and convection was mechanically driven via the forced ascent of conditionally unstable flow (Nugent et al. 2014). Minder et al. (2013) showed the incoming flow experiences minimal lateral deflection when the trades are strong, largely because of latent heat release in the over-island convection. Clouds and convection were concentrated above the upwind slope in the vicinity of leg 3, whereas leg 4 passed through a region of (mostly clear air) turbulence generated by shear instabilities from a plunging flow. The cloudiness fraction was substantially higher along leg 3 on all medium and high wind days (Table 1; Figs. 3c–f), with some bookend convection observed along HIGH-4. A comparison of measurements along MED-3 and HIGH-3 indicate the clouds were deeper, the updrafts stronger, and the LWC higher on high wind days (Fig. 2).

A surprising similarity in the distribution of vertical velocity (w') and LWC emerges along LOW-4 and HIGH-3 (Fig. 2). They share a distinct frequency distribution at the upper end of each variable, with updrafts exceeding 8 m s^{-1} and LWCs approaching the predicted adiabatic value of 2.1 $\pm$ 0.15 g m^{-3} (adiabatic LWC derived from measurements along leg 1L). Therefore, irrespective of how the convection is triggered, cumulus clouds triggered by thermal and mechanical convection appear capable of exhibiting a similar vigor and adiabatic fractions at flight level.

b. Cloud transects

From nearly 100 cloud penetrations, Fig. 4 presents three exemplary cumulus transects above Dominica (note different scale along x axis). They are from a low, medium, and high wind day to illustrate that the cloud morphology changed little from day to day. The upper panels show the cloud radar reflectivity, and overlaid at flight level is the LWC and 2D wind vectors. The lower panels show the corresponding flight-level pressure perturbation (P'), cloud droplet mean volume diameter (MVD), cloud droplet relative dispersion (DD), and the cloud droplet number concentration (NC).

Updrafts above Dominica were almost always cloudy and higher LWCs were often coincident with the strongest updrafts. The observed LWC was always lower than the predicted adiabatic LWC (2.1 $\pm$ 0.15 g m^{-3}), implying that all clouds had experienced some entrainment of environmental air. The strongly flared updrafts

[1] The average cloud-top height is estimated from cloud radar echoes (which distinctly capture growing cumulus turrets above flight level; e.g., Fig. 4), using a threshold of −20 dBZ and the five tallest clouds along each flight leg (to account for differences in cloud maturity).

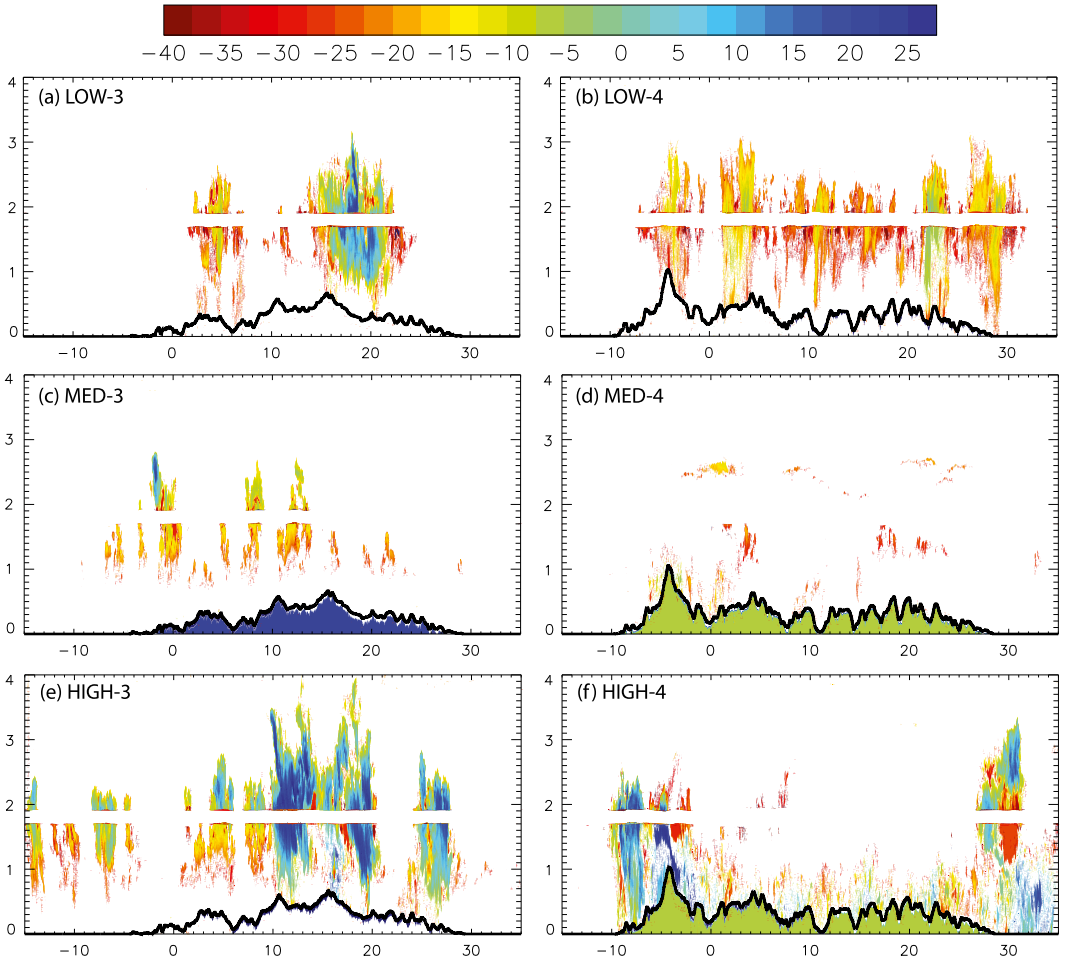

FIG. 3. Examples of over-island cloud radar reflectivity ($\lambda = 3160\ \mu$m) during (a),(b) low, (c),(d) medium, and (e), (f) high wind research flights along (left) leg 3 and (right) leg 4. Each panel shows radar reflectivity (filled contours; dB $\times 10 \log_{10}$; see color bar for scaling) and terrain height (thick black line). See Fig. 1 for approximate location of transects.

and adjacent, strong downdrafts evident in Fig. 4 are reminiscent of the shedding thermal proposed by Blyth et al. (1988). Such a cloud circulation is said to facilitate the organized entrainment of ambient air into the thermal base causing regions of severely depleted LWC, or cloud holes, within otherwise cloudy updrafts (e.g., at $x = 8.5$ km in Fig. 4b and possibly at $x = 4.3$ km in Fig. 4c, although this may have been formed by two adjacent thermals). Entrainment, however, is not a uniform process (Romps and Kuang 2010) and the modeling results of Krueger et al. (1997) suggest in-cloud fractions of clear air exist because of discrete entrainment events and non-instantaneous mixing. Cloud cores with converging updrafts were also observed (not shown), consistent with observations from previous studies of shallow cumulus (e.g., Blyth et al. 2005).

The cloud droplet MVD, the number concentration, and droplet dispersion vary by only small amounts across each cloud transect (with exception to regions where the LWC is very low, such as cloudy downdrafts and cloud holes). These broadly uniform distributions sometimes vanish within subsequent 10-Hz measurements (around 9 m); other transects reveal a more gradual depletion. Determining the dominant mechanism that entrains dry air into the cloud core (e.g., lateral versus cloud top-to-bottom entrainment) and whether subsequent in-cloud evaporation is homogeneous or inhomogeneous is difficult because of the high humidity of the ambient air (e.g., Jensen et al. 1985), the potentially erroneous temperature measurements, and measurements over the island being made at only one altitude.

c. *Cloudy updraft cores*

To compile statistics on the convection above Dominica with different wind speeds, cloudy updraft cores are identified along flight legs within the vicinity of convection

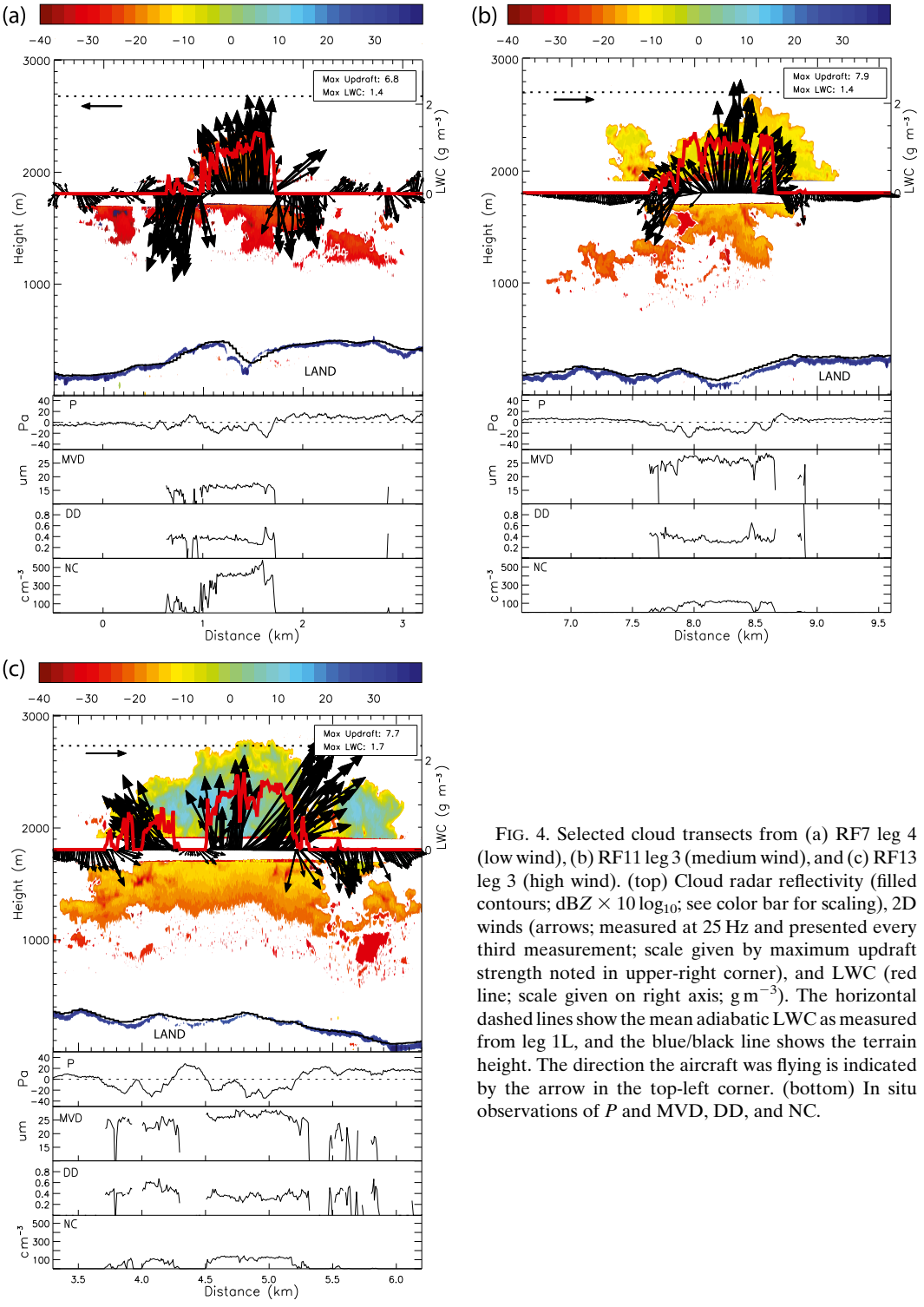

FIG. 4. Selected cloud transects from (a) RF7 leg 4 (low wind), (b) RF11 leg 3 (medium wind), and (c) RF13 leg 3 (high wind). (top) Cloud radar reflectivity (filled contours; dB$Z \times 10\log_{10}$; see color bar for scaling), 2D winds (arrows; measured at 25 Hz and presented every third measurement; scale given by maximum updraft strength noted in upper-right corner), and LWC (red line; scale given on right axis; g m^{-3}). The horizontal dashed lines show the mean adiabatic LWC as measured from leg 1L, and the blue/black line shows the terrain height. The direction the aircraft was flying is indicated by the arrow in the top-left corner. (bottom) In situ observations of *P* and MVD, DD, and NC.

(LOW-3, LOW-4, MED-3, and HIGH-3). A cloudy updraft core (or cloud core) is hereby defined as at least 100 m of contiguous 10-Hz in-cloud measurements with updrafts of $w' \geq 1\,\mathrm{m\,s^{-1}}$, where an in-cloud measurement has a CDP droplet concentration greater than 10 cm^{-3}. To account for small-scale turbulent fluctuations and small cloud holes, cloudy updrafts may be absent over a length no greater than 25 m, the total of which must

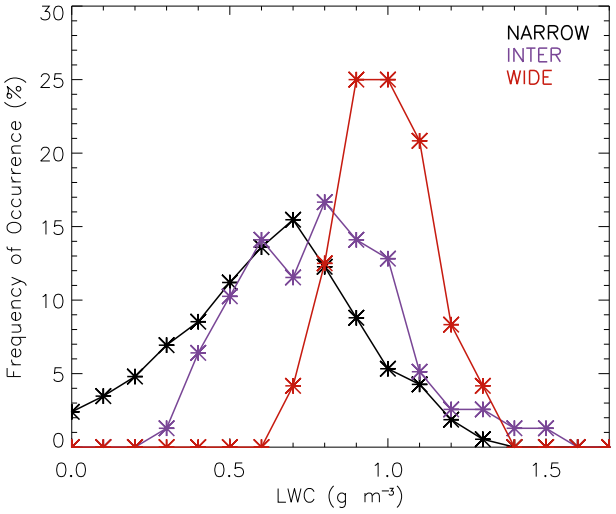

FIG. 5. Frequency distribution of the average LWC for cloudy updraft cores with widths < 500 (black), 500–1000 (magenta), and >1000 m (red). Compiled using flight-level measurements (at z = 1.8 km) from legs 3 and 4 on low wind days and leg 3 on medium and high wind days. The predicted adiabatic LWC is 2.1 g m^{-3}.

constitute less than 10% of the cloud-core width. The total number of cloud cores identified is somewhat sensitive to this definition; however, other statistics (e.g., the average and maximum core width, updraft strength, and LWC) do not significantly change. We are mindful that a low bias in the observed cloud-core width may occur as the aircraft is unlikely to penetrate through the center of every cumulus cloud. Furthermore, the formation of cloud holes wider than 25 m affects identification.

For comparison, cloud-core statistics from the upstream leg 1H are also included. The overocean leg 1H was flown at z = 1.2 km, 500 m below the over-island legs. Only four cloud cores were observed along leg 1H in the seven research flights examined here, all on high wind days.

The widest cloud core observed over Dominica was 1.6 km along LOW-4, and several cloud cores wider than 1 km were also observed along HIGH-3. The overwhelming majority of cloud cores were less than 500 m wide. Figure 5 presents the frequency distribution of the average LWC of cloud cores with three different widths: <0.5, 0.5–1.0, and >1.0 km. The average LWC increases with cloud-core width, which can be understood through the classical quantitative description of the vertical mass flux and entrainment:

$$\frac{1}{M}\frac{\partial M}{\partial z} = \varepsilon \sim \frac{1}{R}. \qquad (1)$$

Here, $M = \rho w_c a_c$ is the upward mass flux (a product of the density ρ, the cloudy updraft velocity w_c, and the cloudy updraft fractional area a_c), ε is the fractional entrainment, and R is the radius of the rising plume.

Equation (1), which originated from laboratory water tank experiments (see, e.g., Morton et al. 1956; Batchelor 1967), is valid under nonbuoyant, nonaccelerating conditions where entrainment is the only process affecting the plume radius. It shows that wider plumes have a smaller fractional entrainment because of their smaller perimeter-to-volume ratio (de Rooy et al. 2013). By extension, wider cloud cores become less diluted by environmental air as they rise through the atmosphere. While this description of the vertical mass flux is crude in consideration of cumulus convection, the observed positive relationship between core width and LWC is consistent with the large-eddy simulations of shallow, orographic cumulus by Kirshbaum and Grant (2012). Of relevance, their results suggest the increased LWC of broader, orographic cumulus can lead to a sharp enhancement in precipitation efficiency (called the "cloud size" mechanism).

Figure 6 presents a range of statistics for cloud cores of different width (the largest width bin includes all cloud cores wider than 1 km). The abundance of narrow cloud cores is evident, especially on the low wind days (Fig. 6a). Consistent with Kirshbaum and Grant (2012), wider cloud cores typically have higher LWCs and stronger updrafts (Figs. 6b,c). Given a predicted adiabatic LWC at flight level of 2.1 g m^{-3}, the widest cloud cores along LOW-4 and HIGH-3 have an adiabatic fraction of 50%–70%. This is double that of the four cloud cores observed upstream along leg 1H—a flight leg that is also closer to cloud base—highlighting the strong orographic/land effect on cumulus development. The orographic cumulus clouds also have substantially higher adiabatic fractions than the shallow trade wind cumulus observed during the RICO experiment (Rauber et al. 2007). For example, Fig. 2 in Blyth et al. (2013) shows the adiabatic fraction during RICO never exceeded 40% when 1 km above the cloud base—the approximate height of legs 3 and 4 in DOMEX. Irrespective of how convection is triggered over Dominica, these results strongly suggest orographic, shallow cumulus clouds are less diluted than those over the open ocean.

The primary difference between MED-3 and HIGH-3 in Fig. 6 is the absence of cloud cores wider than 800 m on medium wind days. This may be due to the weaker mechanical ascent on medium wind days, which appears to affect the development of wider cloud cores rather than the dynamics of narrower cloud cores. Along LOW-3, cloud cores have the weakest updrafts and smallest LWCs of any of the over-island flight legs.

Finally, unlike updraft strength and LWC, the cloud droplet MVD is insensitive to core width or leg number. The cloud cores above Dominica on low wind days have cloud droplets consistently 10 μm smaller (Fig. 6d) and up to 4 times more numerous (not shown). The droplet

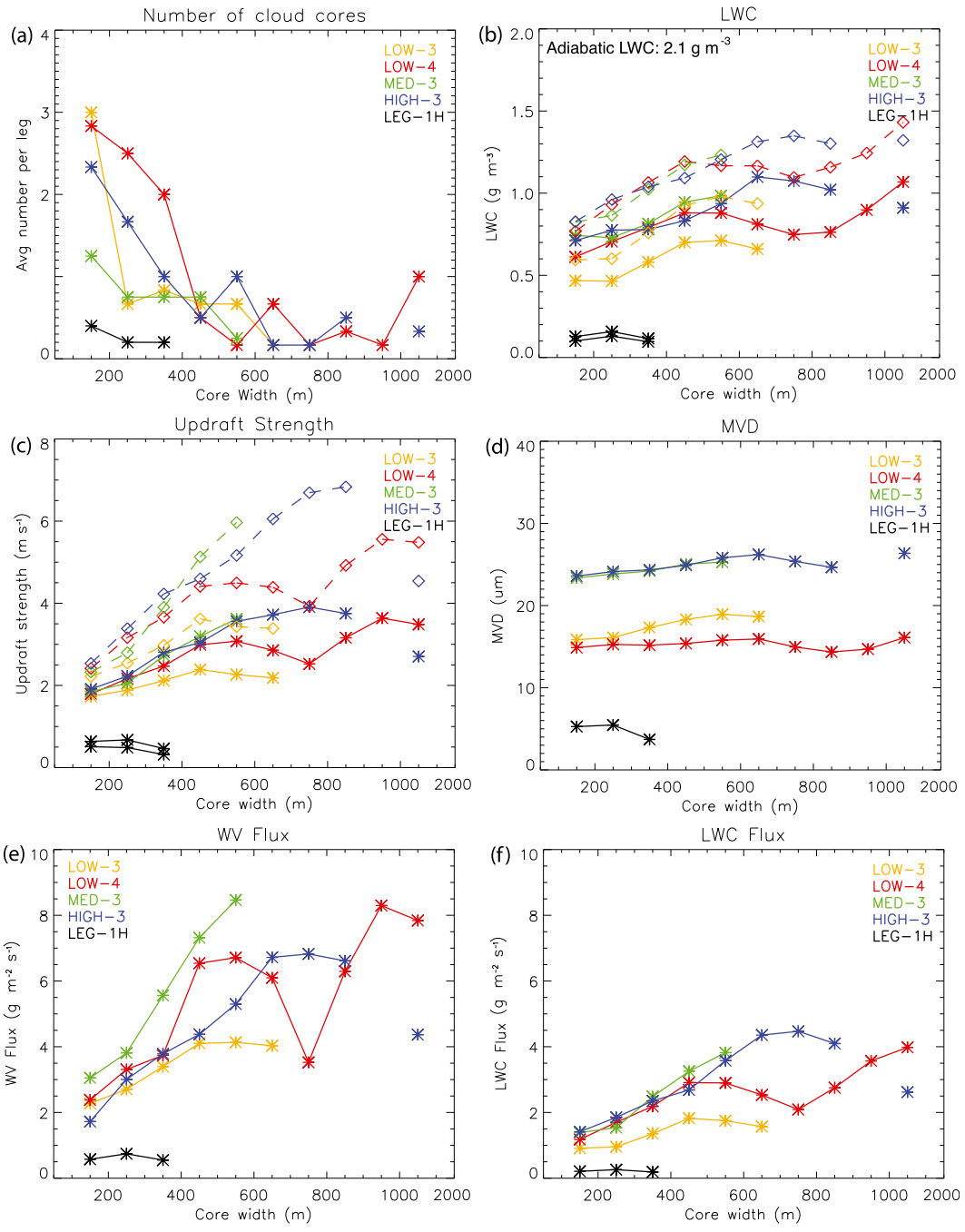

FIG. 6. Cloudy updraft core statistics for different cloud-core widths over and upstream of Dominica. Cloud-core widths are binned every 100 m with the largest bin containing cloud cores wider than 1 km. Solid lines with asterisks show the average value for each cloud-core width; dashed lines with diamonds show the maximum value for each cloud-core width.

MVD therefore appears unaffected by the strength, prevalence, or scale of convection, only the triggering mechanism. This is supported by the average cloud radar reflectivity intensity above flight level (Table 1) and is also consistent with the hypothesis of Smith et al. (2012) that smaller cloud droplets on low wind days are caused by lofting of additional island-derived aerosol into the clouds by thermally driven convection. The absence of giant sea-salt aerosol on low wind days may also have some effect (see section 5).

TABLE 2. Selected statistics for leg-average vertical fluxes, calculated using the formulas in the left column. Here, L is total leg distance; dx is the integral length (or distance between observations); w' is the perturbation vertical velocity; ρ is density; q' and q'_c are the perturbation water vapor and cloud water specific humidities, respectively; T' is the perturbation temperature; l_v is the latent heat of vaporization; and c_p is the specific heat capacity of dry air/water vapor for cloudy/noncloudy air.

	Units	Leg	RF7, -8 (low)	RF11, -18 (medium)	RF12, -13, -17 (high)
Wind speed	$m\,s^{-1}$	1L	2.9	6.6–7.0	9.1–11.4
Latent heat flux: $\frac{l_v}{L}\int \rho w' q'\,dx$	$W\,m^{-2}$	1L	106	133	106
		1H	−34	34	31
		3	331	463	**675**
		4	**1485**	297	272
Sensible heat flux: $\frac{c_p}{L}\int \rho w' T'\,dx$	$W\,m^{-2}$	1L	−2.6	0.6	0.8
		1H	2.6	−4.7	1.5
		3	3.7	114.3	**146.9**
		4	**236.5**	17.6	153.4
Liquid water flux: $\frac{1}{L}\int \rho w' q'_c\,dx$	$g\,m^{-2}\,s^{-1}$	1L	—	—	—
		1H	2.1×10^{-5}	1.3×10^{-7}	0.01
		3	0.06	0.13	**0.19**
		4	**0.33**	0.05	0.06

d. *Vertical fluxes*

While convection over the island is of two types (thermal and mechanical), both are clearly more frequent, vigorous, and closely packed than the convection over the open ocean. Table 2 presents the leg-average vertical fluxes of moisture, heat, and mass along the upstream and over-island legs. In general, the latent heat flux (LHF) is substantially larger than the sensible heat flux (SHF) indicating the dominant role of moist convection. Note that in-cloud temperature measurements may be affected by wetting; the SHF could be underestimated along flight legs in the cloud layer.

Upstream of Dominica, the subcloud (leg 1L) fluxes have values consistent with those obtained during RICO (Rauber et al. 2007; Nuijens et al. 2009) and from bulk theory for the trades (Nuijens and Stevens 2012). The over-island fluxes are often an order of magnitude larger than those upstream, with the strongest fluxes occurring along flight legs within the vicinity of convection. The leg-average fluxes along LOW-4 are almost twice as large as HIGH-3, although this is partly due to LOW-4 having around 30% more cloud cores (the average cloud-core vertical flux of water vapor and liquid water is roughly equal along LOW-4 and HIGH-3; Figs. 6e,f). Flux profiles cannot be derived as observations at other altitudes above Dominica are not available.

Aircraft measurements show some significant differences in the vertical flux of heat and moisture between thermally and mechanically driven convection (Table 2). The impact of this difference on precipitation is presently unknown; however, the results presented hitherto suggest the convection triggered by Dominica on low wind days is equally (if not more) energetic and widespread at flight level than on high wind days. Moreover, the characteristics of the cloud cores observed at flight level are remarkably similar, irrespective of how they are triggered (with exception to the cloud droplet spectrum, which may be related to an aerosol effect; see section 5).

4. The ambient environment

While the orographic cumulus clouds on low and high wind days during DOMEX share many similar characteristics at flight level, they are consistently shallower on low wind days (by an average of 500 m, assuming negligible cloud base variation). Indeed, a relationship between trade wind speed and cumulus depth has been appreciated for some time (e.g., Austin 1948), and recent work by Nuijens and Stevens (2012) using bulk theory arguments suggests when the trades weaken, the inversion height decreases, which makes the cloud-layer shallower. In turn, the cloud-top LWC should fall, perhaps reducing the likelihood of the cloud precipitating. This forms the basis of the second hypothesis.

a. *The ambient environment during DOMEX*

Vertical profiles from the upwind soundings of the seven research flights are presented in Fig. 7. They show the wind speed toward Dominica (u), virtual temperature (T_v), equivalent potential temperature (θ_e), and relative humidity (RH; all at 25 Hz). The profiles are color coded according to their ambient trade wind speed class. We stress these measurements are from upstream of Dominica and not necessarily representative of the over-island environment.

In the marine boundary layer, the low wind days were cooler and drier than the medium and high wind days; the RH, however, was roughly equal. Cloud base formed

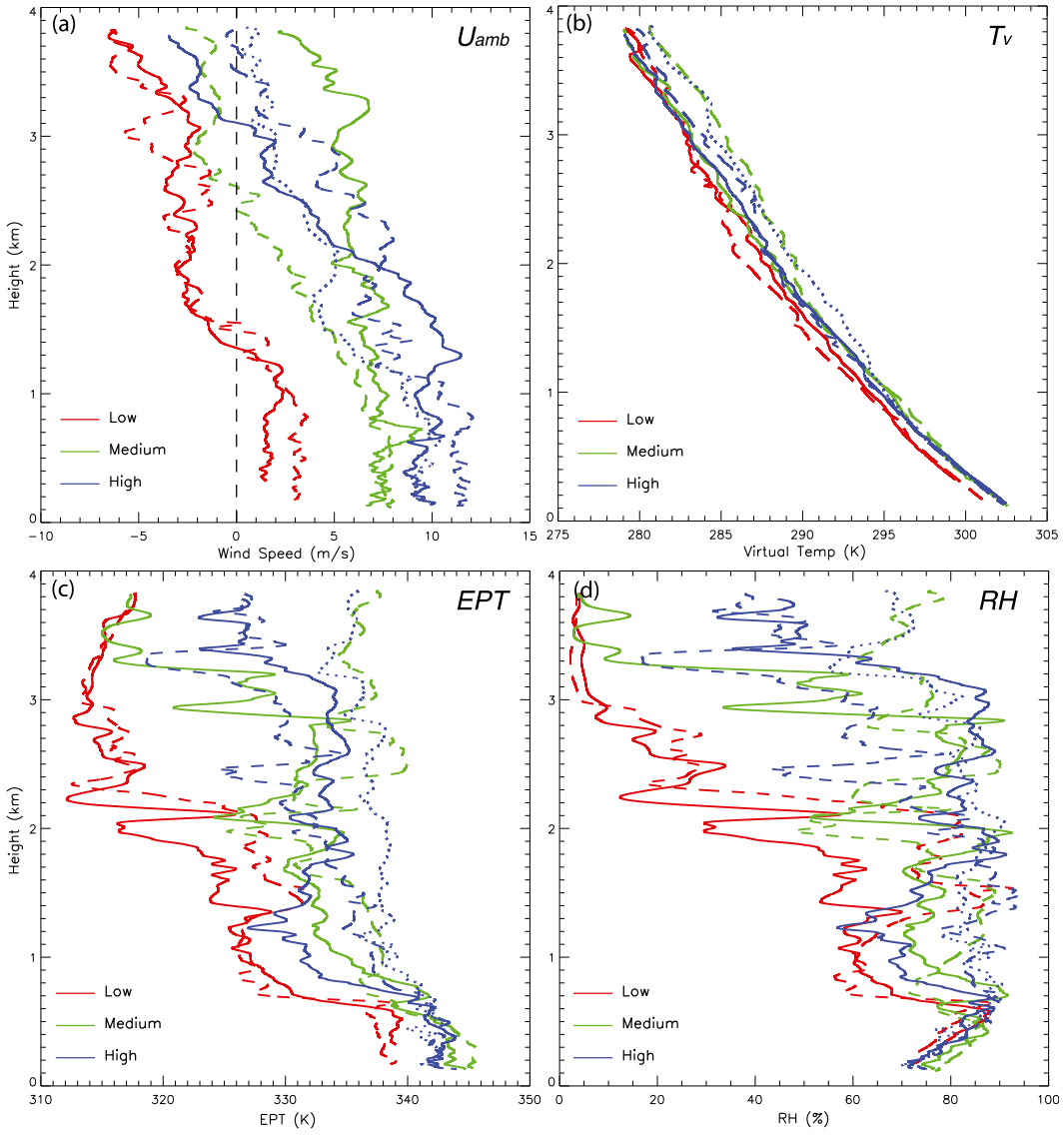

FIG. 7. Vertical profiles measured during the upstream sounding by the aircraft of (a) u wind speed ($\mathrm{m\,s^{-1}}$), (b) virtual temperature (K), (c) equivalent potential temperature (K), and (d) relative humidity (%) for RF7 (blue solid line), RF8 (blue dashed line), RF11 (green solid line), RF18 (green dashed line), RF12 (red solid line), RF13 (red dashed line), and RF17 (red dashed line). These profiles have been smoothed from 25 to 0.25 Hz.

somewhere around 700 m each day, estimated from the attenuation of the upward-pointing lidar and the lifting condensation level predicted from in situ measurements along leg 1L. No measurements of cloud base above the island are available.

It was notably drier in the lower free troposphere on low wind days: immediately above the boundary layer, there was a sharp drop in humidity, followed by another drop in humidity around z = 1.8–2.3 km, which likely coincides with the trade wind inversion. On the medium and high wind days, the RH remained between 50% and 80% up to z = 3–4 km. In other words, the upstream cloud layer was drier and shallower on the low wind days.

The θ_e profiles reflect these variations in moisture and are reminiscent of the observed θ_e profiles from Barbados (north of Dominica) in Aspliden (1976, his Fig. 1). He noted an energy (or θ_e) minimum in the lower free troposphere typically intensified and descended during periods of depressed convection in the trades, and the opposite occurred during periods of deeper convection. Humidity changes were considered to be almost exclusively responsible for these energy changes. The low wind days during DOMEX appear characteristic of

these periods of depressed convection, consistent with the lower cloudiness fraction upwind (Table 1).

Each drop in humidity was accompanied by an increase in temperature, hence the vertical gradient of T_v was comparable for each research flight. This buoyancy adjustment has the effect of increasing the dry static stability in drier regions while keeping the moist static stability unchanged (and is important in the development of the idealized soundings in section 4d; see also appendix A). This makes identifying the presence and height of the trade wind inversion difficult, which based on the relative humidity appears to be around $z = 2$ km on the low wind days and $z > 3$ km on high wind days (if present at all). We note Davison et al. (2013b) and Davison et al. (2013c) propose a more robust method to define the trade wind inversion using the Braggs scattering layer, which we have not tested here.

b. A climatology of the ambient environment from Guadeloupe

Although DOMEX included many events, the dataset is not long enough to give statistically robust results. We therefore use soundings from the neighboring island of Guadeloupe in April and May (the months of the field campaign) from 2000 to 2013. These soundings were made most days from Guadeloupe airport at 1000 local time, and while the lowest levels of the sounding are affected by surface properties, comparison to the upwind profiles observed during DOMEX indicate the Guadeloupe soundings prove a valid measure of ambient conditions above about 500 m for thermodynamic variables and 700 m for winds (Nugent et al. 2014).

We categorize the Guadeloupe soundings into those with low or high wind speed conditions and dry or moist cloud layers. For this, we use the 925-hPa wind speed [both perpendicular to the island (U_{P925}) and its total magnitude (U_{T925})]. Low wind conditions are defined as $U_{P925} > -2\,\mathrm{m\,s^{-1}}$ and $U_{T925} < 5\,\mathrm{m\,s^{-1}}$, and high wind conditions are defined as $U_{P925} > 7\,\mathrm{m\,s^{-1}}$ and $U_{T925} < 15\,\mathrm{m\,s^{-1}}$. For the humidity of the cloud layer, we use the average relative humidity from 1.5 to 3 km ($\mathrm{RH_{mid}}$). A dry cloud layer is defined as $\mathrm{RH_{mid}} < 40\%$, and a moist cloud layer is defined as $\mathrm{RH_{mid}} > 60\%$.

The choice of these thresholds is motivated by the upwind profiles measured during RF7 and RF8 (low wind days with drier cloud layers) and RF12, RF13, and RF17 (high wind days with moister cloud layers). While there is some variation in the observed soundings within the three wind speed classes (e.g., RF8 is more moist than RF7 from $z = 1.5$ to 2 km), it is not our intention to perform an exhaustive analysis of the thermodynamic environment [which exhibits significant and complex variability; see, e.g., Davison et al. (2013a)].

TABLE 3. Statistics from 803 balloon soundings at Guadeloupe in April and May from 2000 to 2013. See section 4b for details. All values are percentages.

925-hPa wind speed conditions:	Low wind	High wind
Frequency of occurrence	20.3	29.3
Frequency when dry/moist	16.0/43.0	8.9/64.2
Relative humidity of cloud layer:	**Dry**	**Moist**
Frequency of occurrence	15.6	49.3
Frequency when low/high wind	20.8/17.7	16.8/38.1

Of the 803 available soundings, 29% have high wind conditions and 20% have low wind conditions (Table 3). When wind conditions were high, the cloud layer was much more likely to be moist (64%) than dry (9%). When wind conditions were low, dry conditions became more frequent (16%) although the cloud layer was still more likely to be moist (43%). Accordingly, the cloud layer was moist (50%) more frequently than it was dry (16%), with a moist cloud layer more than twice as likely to be associated with high wind conditions. This is generally consistent with the conditions observed during the DOMEX field campaign.

While simple, this analysis reflects our interest in the broad relationship between the trade wind speed, the inversion height, and cloud-layer depth. As in previous work (e.g., Nuijens et al. 2009; Nugent et al. 2014), we cannot find a statistically significant relationship between cloud-layer moisture and trade wind speed. The dry condition aloft during the two low wind days of DOMEX appears climatologically exceptional and occurs almost as frequently during high wind conditions.

c. A simple entraining parcel model

Through dry-air entrainment, the properties of the surrounding environment have a significant influence on the fate of each cumulus cloud. To measure this influence, we use a simple entraining parcel model. While highly idealized, a parcel model shows how a parcel lifted from the boundary layer is affected by its ambient environment. It assumes the moist static energy (MSE) of a uniform, well-mixed parcel is conserved upon ascent, where MSE is given by

$$\mathrm{MSE} = (c_{\mathrm{pd}} + r_t c_l)T + L_v r_v + (1 + r_t)gz, \qquad (2)$$

and r_t and r_v are the total water and water vapor mixing ratios, T is temperature, z is height above sea level, c_{pd} and c_l are the heat capacities of dry air (at constant pressure) and liquid water, L_v is the latent heat of vaporization, and g is gravitational acceleration. We assume the parcel is spherical with an initial radius (R) and volume (V). The volume increases with height based on

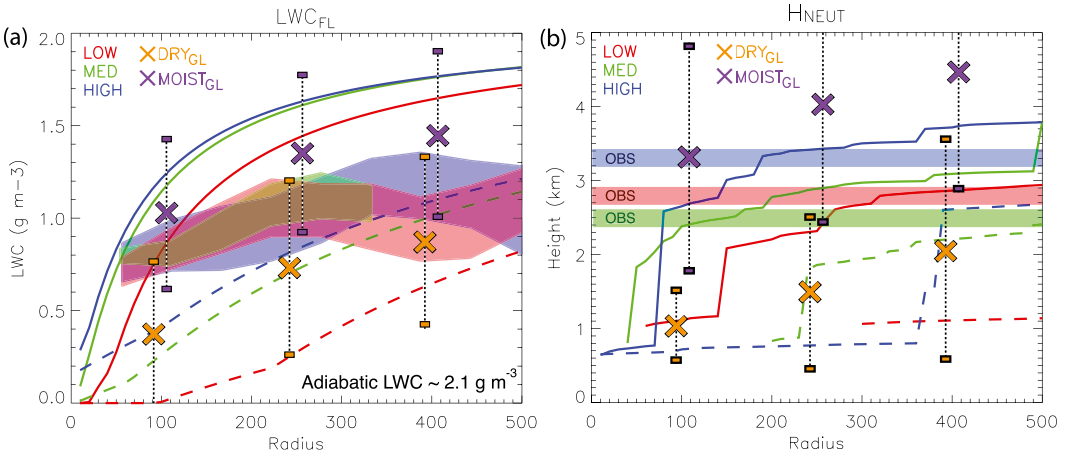

FIG. 8. A simple entraining parcel model illustrating the influence of the environment on a parcel of varying radius, lifted from $z = 500$ m to 5 km. (a) $\mathrm{LWC_{FL}}$ and (b) H_{neut}. The environment is represented by the low, medium, and high wind DOMEX profiles (red, green, and blue, respectively) and the $\mathrm{Dry_{GL}}$ and $\mathrm{Moist_{GL}}$ cloud-layer soundings from Guadeloupe (orange and magenta). For the DOMEX profiles, $\alpha_E = 0.1$ (solid lines) and 0.5 (dashed lines), and R increases from 10 to 500 m in 10-m increments. Results from each wind speed class are averaged for clarity. For the Guadeloupe soundings, $\alpha_E = 0.1$ and $R = 100$, 250, and 400 m. The × symbol represents the mean and the vertical dotted lines represent one standard deviation from the mean. For reference, the shaded regions indicate the observed cloud-core LWC (bound by the average and the average-maximum cloud-core LWC; see Fig. 6b) and the average cloud-top height along LOW-4, MED-3, and HIGH-3.

its fractional expansion rate (ψ) and entrainment (α_E), such that $dV/dz = V\psi + \alpha_E(\pi R^2 dz)$. As in Morton et al. (1956), the volume of entrained air is related only to dz and R, with α_E acting as the proportionality constant of dilution. The entrained air is mixed instantaneously and uniformly within the parcel, such that

$$\mathrm{Mass}_1\mathrm{MSE}_1 + \mathrm{Mass}_2\mathrm{MSE}_2 = \mathrm{Mass}_3\mathrm{MSE}_3 \quad \text{and} \tag{3}$$

$$\mathrm{Mass}_1(q_v + q_l)_1 + \mathrm{Mass}_2(q_v + q_l)_2 = \mathrm{Mass}_3(q_v + q_l)_3. \tag{4}$$

Here, subscript 1 denotes the ascending parcel, subscript 2 denotes the entrained environmental air, and subscript 3 denotes the combination of 1 and 2; q_v and q_l are the specific humidities of water vapor and liquid water, respectively. Detrainment is neglected for simplicity (the parcel expands as it rises), and ice is not considered as the shallow cumulus clouds above Dominica rarely grow beyond the freezing level.

Four inputs are required to initialize the parcel model: R, α_E, the initial height of the parcel, and the environmental profile. Each parcel is lifted to $z = 6$ km. While there are numerous ways to analyze parcel evolution, for comparison to observations we focus on the total LWC of the parcel at flight level above the island ($\mathrm{LWC_{FL}}$) and the highest level of neutral buoyancy of the parcel relative to the surrounding environment (H_{neut}, a proxy for the cloud-top height). While $\mathrm{LWC_{FL}}$ is affected only by the environment below flight level ($z = 1.8$ km), H_{neut} can also be affected by conditions further aloft (i.e., the height of the trade wind inversion can be important).

Although some convective parameterization schemes continue to use one-dimensional models based on the Morton et al. (1956) entraining plume model (de Rooy et al. 2013), we are mindful it is an oversimplification of the entrainment and mixing process (e.g., Neggers et al. 2002; Siebesma et al. 2003; Nie and Kuang 2012). Moreover, entrainment is never identical; Romps and Kuang (2010) suggest some parcels entrain very little while others with similar initial properties suffer the opposite fate.

1) THE PARCEL MODEL WITH UPWIND PROFILES FROM DOMEX

The solid and dashed lines in Fig. 8 show how $\mathrm{LWC_{FL}}$ and H_{neut} change as parcels of different radii are lifted through the seven upwind profiles observed during DOMEX (results have been averaged within each wind speed class). Each parcel is lifted from $z = 300$ m and the initial radius R is increased from 50 to 500 m. To illustrate the effect of entrainment, two values of α_E are used: $\alpha_E = 0.1$ (solid lines; the approximate value obtained by Morton et al. 1956) and $\alpha_E = 0.5$ [dashed lines; used by Sherwood et al. (2013) in experiments where drag forces were neglected to represent a "slippery thermal"; see their section 4].

Both $\mathrm{LWC_{FL}}$ and H_{neut} increase with R, and this increase is more rapid when R is small (the stepped increase

in H_{neut} with R is caused by the observed environment having a nonuniform buoyancy profile). This is driven by the Morton et al. (1956) formulation of entrainment that ensures wider parcels have a lower fractional entrainment, consistent with the simple mass flux equation presented earlier [Eq. (1)]. The parcel model also captures the observed increase in LWC with cloud-core width to some degree.

The medium and high wind (i.e., moist) environments promote a higher LWC_{FL} and H_{neut} than the low wind (i.e., dry) environment, especially when entrainment is strong. This positive correlation between LWC_{FL} and H_{neut} is expected because a lower LWC_{FL} implies increased evaporation, cooling, and thereby a reduction in buoyancy. While H_{neut} is generally comparable to the observed average cloud-top height when $\alpha_E = 0.1$—especially for wider parcels in the low and high wind environments—LWC_{FL} is unrealistically high: the adiabatic fraction of wider parcels 1 km above the cloud base exceeds 80%.

When $\alpha_E = 0.5$, no parcels with $R < 300$ m achieve positive buoyancy in the low wind environment (H_{neut} is undefined) whereas LWC_{FL} is closer to observations. The stronger entrainment therefore promotes a more realistic LWC; however, in doing so, it excessively reduces parcel buoyancy. This same issue was noted by Warner (1970), who said it was impossible for such a model to simulate both the LWC and cloud-top height of individual cumulus when the rising parcel is diluted through lateral entrainment only (as it is in this idealized model).

Another conflict between observations from DOMEX and results from the parcel model is that the observed LWC at flight level remains largely unchanged on low and high wind days. In contrast, LWC_{FL} of a parcel in the low wind environment is notably less than in the medium and high wind environments (especially when $\alpha_E = 0.5$). This highlights an issue of comparing results from the parcel model to observations above Dominica: it is only valid if the upwind profiles observed during DOMEX are representative of the environment above Dominica. It could be argued that when the trades are strong, the upwind profiles are a fair representation of the over-island conditions. However, on low wind days the environment continually evolves as the weak trades fail to flush out the effects of diurnal–thermal convection (e.g., Zehnder et al. 2009). A comparison of out-of-cloud observations along legs 3 and 4 to the upwind profiles on low wind days shows a moister above-island cloud layer.

2) THE PARCEL MODEL WITH SOUNDINGS FROM GUADELOUPE

To provide a climatological perspective on the factors controlling LWC_{FL} and H_{neut}, the Guadeloupe soundings with dry cloud layers (Dry_{GL}) and moist cloud layers ($Moist_{GL}$) are used as environmental profiles in the parcel model (see section 4b for how the Guadeloupe soundings are categorized). The mean $LWC_{FL–GL}$ and mean $H_{neut–GL}$ for the two categories of Guadeloupe soundings are overlain in Fig. 8: the orange crosses are for the Dry_{GL} soundings, and the magenta crosses are for $Moist_{GL}$ soundings. For simplicity, $LWC_{FL–GL}$ and $H_{neut–GL}$ are only calculated with $\alpha_E = 0.1$ and $R = 100$, 250, and 400 m, and the Guadeloupe soundings are linearly interpolated to 1 m (for iteration purposes). Note the substantial spread in the results, indicated by the vertical dotted lines.

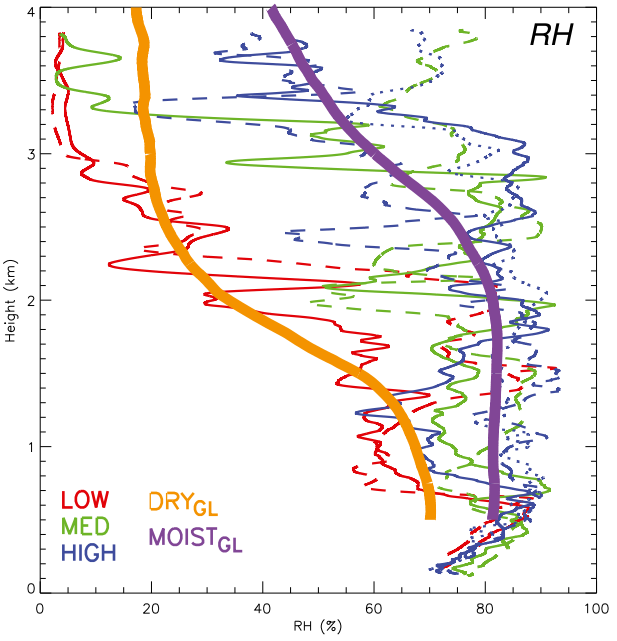

FIG. 9. Vertical profiles of the RH from the upwind aircraft soundings from DOMEX (thin lines) and the mean RH_{GL} from the Guadeloupe soundings (thick lines). The thin red lines are for low wind days RF7 and RF8, the thin green lines are for medium wind days RF11 and RF18, and the thin blue lines are for high wind days RF12, RF13, and RF17. The thick orange line is for the Dry_{GL} soundings from Guadeloupe, and the thick magenta line is for the $Moist_{GL}$ soundings.

While both RF7 and RF8 were considered to be relatively dry in the context of DOMEX, the parcel model shows they promote a much greater LWC_{FL} than the mean $LWC_{FL–GL}$ during "dry" conditions (cf. solid red line to the orange crosses in Fig. 8a). This greater LWC_{FL} is caused by a higher-than-average RH between $z = 1.5$ and 2 km (Fig. 9), with the RH at $z = 2$ km in RF8 being significantly higher than the mean. The cloud-layer depth (inferred from the RH profiles in Fig. 9) also appears several hundred meters deeper than the climatological mean for dry conditions (Dry_{GL}), which promotes a higher H_{neut}.

The conditions observed during DOMEX are clearly not representative of the many thermodynamic states possible in the trade wind region. If a research flight were conducted when the ambient environment produced parcel characteristics lower than the dry climatological mean, would we observe even shallower orographic cumulus over Dominica like the parcel model would predict? And what if the trade winds were strong on this day, forcing mechanical rather than thermal convection over the island? While the parcel model is not adequate to explore such questions owing to its absence of dynamics and the difficulty of constraining α_E, it demonstrates that cloud-layer humidity, cloud size, and dry-air entrainment play an important role in cumulus development over Dominica.

d. Heat bubble simulations using WRF

A conventional tool for investigating atmospheric convection is the mesoscale numerical weather prediction model. Configuring such models to simulate realistic orographic convection over Dominica is not trivial; we therefore attempt to bridge the gap between the parcel model and more realistic numerical simulations by performing a series of highly idealized simulations with the Weather Research and Forecasting (WRF) Model, version 3.5 (Skamarock et al. 2008). This work is limited to exploring how variations in cloud-layer moisture, cloud size, and entrainment affect the development of an individual cloud.

Cumulus clouds are simulated at large eddy-resolving resolution within three idealized environments: Moist, Dry, and Dry_{MOD} (the thick lines in Fig. 10). Here, the Moist and Dry soundings are representative of the upwind profiles observed during DOMEX on high and low wind days, and Dry_{MOD} is representative of how the environment above Dominica may be modified by diurnal–thermal convection based on the leg-average out-of-cloud mixing ratio along LOW-4. Appendix A describes the development of these three soundings, which include an adjustment to the temperature profiles in Dry and Dry_{MOD} to ensure the dT_v/dz is identical to Moist.

A cloud is initialized in each WRF simulation by inserting a 1°C Gaussian heat bubble in the boundary layer at the model start time ($T = 0$). To test the influence of cloud size, the heat bubble has three horizontal radii: $R_B = 375$ m, 750 m, and 1.5 km. To emulate variations in entrainment (as in the parcel model), a second-order horizontal and vertical diffusion is applied to all fields with a prescribed eddy diffusivity rate of $K = 2.5$, 5.0, and 7.5 $\text{m}^2\,\text{s}^{-1}$, giving a mixing distance $d = \sqrt{Kt}$ of around 40, 55, and 70 m over $T = 10$ min.

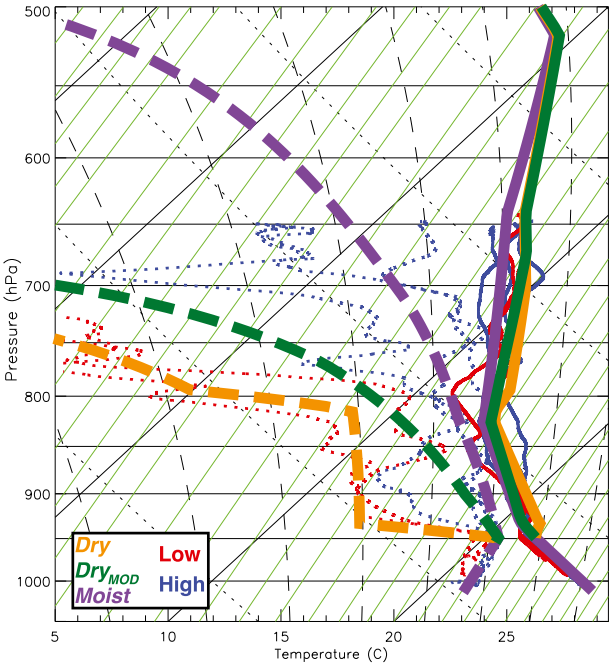

FIG. 10. Skew-T profiles of the idealized environments used in WRF simulations. The Moist (thick purple lines) is based on the upwind soundings on high wind days (thin blue lines); Dry (thick orange lines) and Dry_{MOD} (thick green lines) are based on the upwind soundings and above-island observations on low wind days (thin red lines). See appendix A for details on the development of each sounding.

Each WRF simulation has a horizontal and vertical grid spacing of around 50 m in the lowest 4 km, which should resolve fairly well the energy-containing eddies associated with cumulus convection (e.g., Bryan et al. 2003). Most simulations require $T = 15$–30 min for the cloud to develop and reach its maximum altitude (which was not always above the flight level of $z = 1.8$ km). Further details of the model setup are provided in appendix B.

While orographic effects are not included in these experiments, the choice of a heat bubble with varying horizontal scale reflects our interest in clouds initiated by (i) the bulk ascent of subcloud moisture anomalies during mechanically driven convection (Woodcock 1960; Kirshbaum and Smith 2009; Nugent and Smith 2014) and (ii) surface heating during thermally driven convection (Kirshbaum 2013). Furthermore, the heat bubble is useful in this case as it is not explicitly representative of either convective triggering regime.

1) HEAT BUBBLE IN MOIST ENVIRONMENT

Figure 11 shows four sequential vertical slices through a simulated cloud in the Moist environment when $K = 5\,\text{m}^2\,\text{s}^{-1}$ and $R_B = 1.6$ km. When the cloud

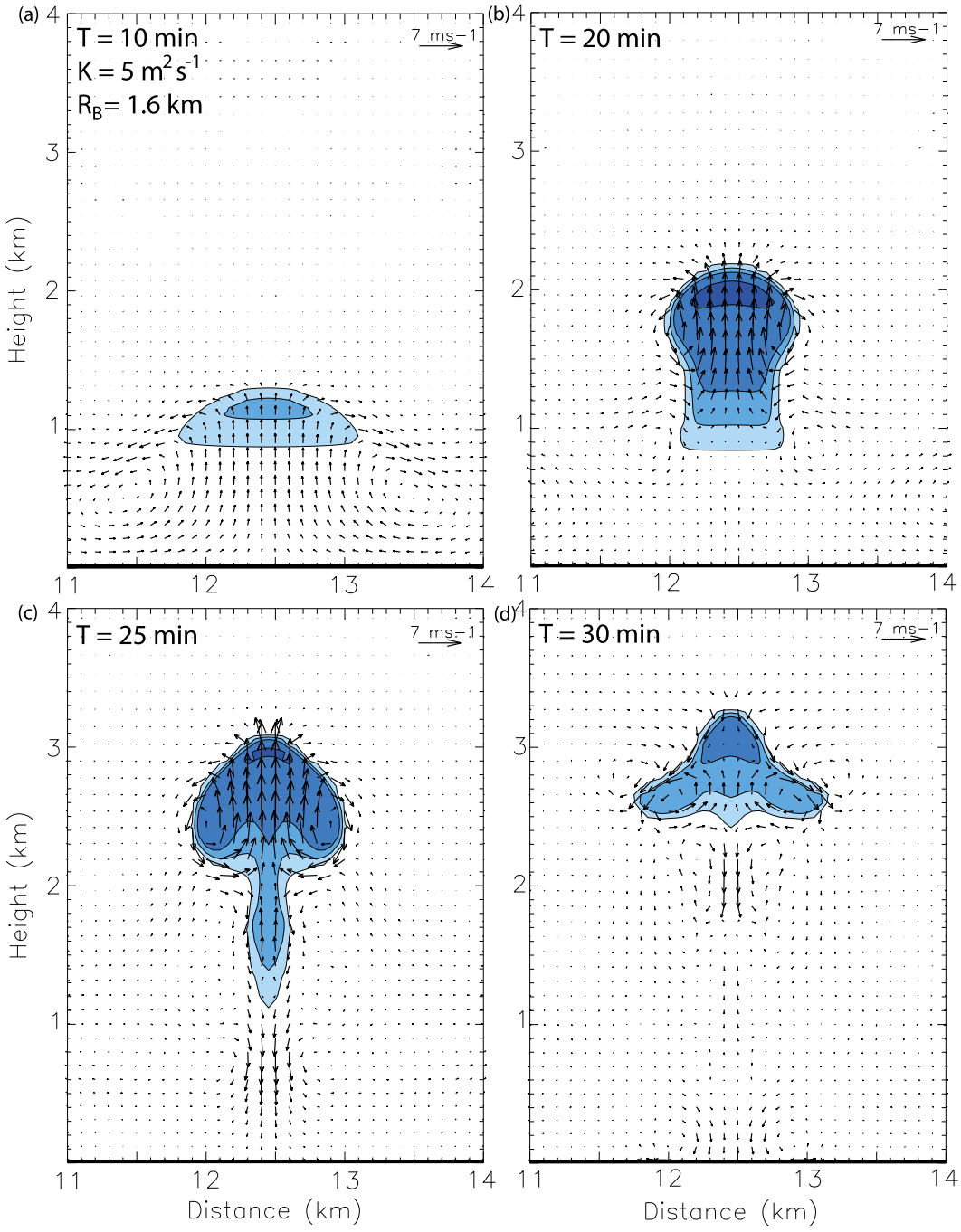

FIG. 11. A simulated cumulus cloud in the Moist environment at different times using $K = 5\,\mathrm{m^2\,s^{-1}}$ and $R_B = 1.6$ km. The grid resolution is 50 m. Each panel shows vertical cross sections through the center of the domain. Plots show LWC (blue-filled contours at 0.1, 0.5, 1.0, 2.0, and 3.0 g $\mathrm{m^{-3}}$ indicated by the lightest to the darkest blue shades) and airflow in the plane of the cross section (vectors; see top right for scaling).

first forms, its diameter is broad (≈1.9 km). As latent heat is released and the cloud cap accelerates, the cloud narrows to conserve mass and the cloud at flight level ($z = 1.8$ km) is less than half the width of the heat bubble that triggered the convection (Table 4). The rising cloud develops a vortical circulation similar to the shedding thermal described in Blyth et al. (1988), and the strong updrafts and adjacent downdrafts resemble the observed cloud transects in Fig. 4. The cloud eventually overshoots its level of neutral buoyancy at the trade

TABLE 4. Flight-level (F.L., $z = 1.8$ km) diagnostics from the WRF Model heat bubble simulations in the (left) Moist and (right) Dry_{MOD} environments. A long dash indicates the cloud did not reach flight level.

Moist	$R_B = 1.6$	$R_B = 0.8$	$R_B = 0.4$	Dry_{MOD}	$R_B = 1.6$	$R_B = 0.8$	$R_B = 0.4$
			Highest, average cloud-core LWC at F.L. (g m^{-3})				
$K = 2.5$	1.62	1.55	1.33	$K = 2.5$	1.60	1.42	—
$K = 5.0$	1.60	1.31	—	$K = 5.0$	1.33	—	—
$K = 7.5$	1.38	—	—	$K = 7.5$	—	—	—
			Corresponding cloud-core radius at F.L. (km)				
$K = 2.5$	0.75	0.40	0.20	$K = 2.5$	0.50	0.25	—
$K = 5.0$	0.65	0.20	—	$K = 5.0$	0.20	—	—
$K = 7.5$	0.35	—	—	$K = 7.5$	—	—	—
			Strongest, average cloud-core updraft at F.L. (m s^{-1})				
$K = 2.5$	4.3	3.6	2.4	$K = 2.5$	4.1	3.0	—
$K = 5.0$	4.5	2.5	—	$K = 5.0$	3.0	—	—
$K = 7.5$	3.6	—	—	$K = 7.5$	—	—	—

wind inversion (around $z = 3$ km), reaching a maximum cloud-top height of 3.4 km at $T = 26$ min.

As R_B and K are varied, the clouds grow to different heights (Fig. 12a). Of the nine clouds simulated in the moist environment with no turbulence, only five grow beyond flight level ($z = 1.8$ km; Table 4). In general, increasing R_B and decreasing K generates wider clouds with stronger updrafts that rise faster and grow deeper (Fig. 12). Of the five clouds that reach flight level, the average cloud-core updraft strength at flight level is comparable to observations (2–5 m s^{-1}), as is the strongest updraft (>6 m s^{-1}). Consistent with results from the parcel model, cloud properties appear most sensitive to changes in R_B and K when R_B is small and K is large; that is, strongly entraining cumulus clouds are more sensitive to variations in their width and entrainment rate when they are narrow.

2) HEAT BUBBLE IN DRY AND DRY_{MOD} ENVIRONMENTS

The adoption of a drier environment has a dramatic impact on cumulus development. No clouds grow beyond 1.2 km in the Dry environment, representative of the observed upwind profile on the low wind days (Fig. 10 and appendix A). Additional simulations show that a heat bubble of 4°C is required to generate a cloud that reaches flight level. This is stronger than the observed 3°C surface warming observed on Dominica on low wind days (Nugent et al. 2014), implying thermally driven convection must precondition the above-island environment for cumulus development.

In the Dry_{MOD} environment (Fig. 10), three clouds grow beyond flight level, all of which have a maximum cloud-top height lower than in the Moist environment

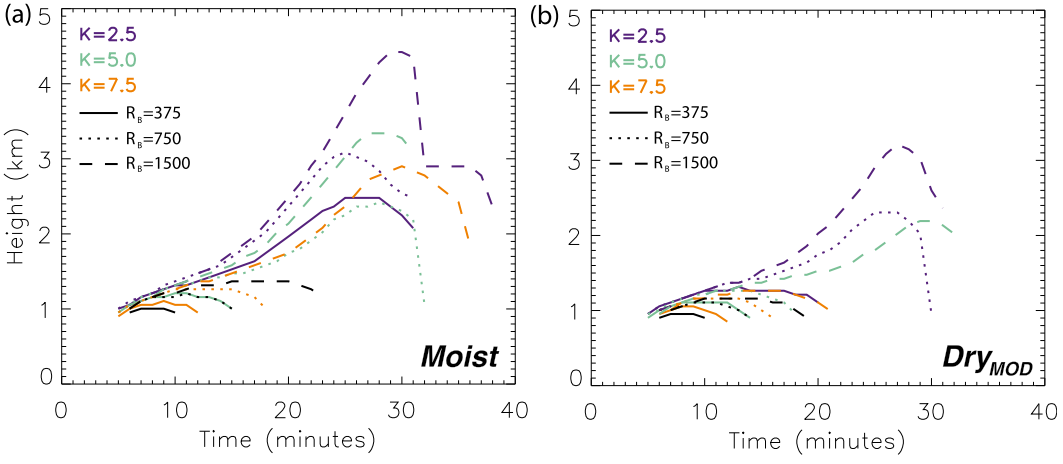

FIG. 12. The time evolution of the maximum cloud-top height from WRF simulations in the (a) Moist and (b) Dry_{MOD} environment when convection is triggered by a heat bubble with horizontal radii $R_B = 375$ m, 750 m, and 1.5 km; and prescribed eddy diffusivity rates of $K = 2.5$, 5.0, and 7.5 $\text{m}^2\,\text{s}^{-1}$.

(Fig. 12b). Neither the cloud width, LWC, or updraft strength is greatly affected at flight level, suggesting the greatest effects on cumulus development occur above this altitude at the trade wind inversion (at $z \approx 2$ km in Dry_{MOD}).

While limited in scope, these simulations suggest two important properties of the orographic cumulus over Dominica. First, the drier environment has a pronounced impact on cloud depth through dry-air entrainment. Even in the modified Dry_{MOD} environment, clouds fail to reach the heights of those in the moist environment. While Kirshbaum and Grant (2012) did not find an increase in precipitation with cloud depth in their idealized simulations, we believe the impact of additional LWC in deeper clouds within more moist environments warrants further examination.

Second, wider clouds are more robust than narrow clouds: the increased size protects the interior core region from entrained environmental air, allowing them to be less sensitive to variations in the environmental conditions. This is relevant to precipitation on Dominica because wider cores with higher LWCs may improve precipitation efficiency in shallow cumulus clouds (Kirshbaum and Grant 2012). However, the model shows simulated LWC is significantly more sensitive to cloud width than the observed LWC. Furthermore, observations during DOMEX indicate low and high wind days have a similar distribution of cloud sizes at flight level over the island. The cloud-size mechanism therefore appears unlikely to be the cause of the sharp reduction in precipitation when convection is thermally driven.

5. Sea-salt aerosol in the marine boundary layer

The third hypothesis explored in this paper—that sea-salt aerosol exert some control on precipitation over Dominica—relies on the premise that (i) the concentration of sea-salt aerosol varies primarily because of wind speed-dependent wave breaking, with higher concentrations observed when surface winds are strong (e.g., Woodcock 1953), and (ii) giant (radius $> 0.5\,\mu$m), hygroscopic aerosol are important to the onset of the coalescence process in shallow cumulus and the initial development of precipitation (e.g., Johnson 1982; Cooper et al. 1997; Jensen and Lee 2008). As the presence of sea-salt aerosol in and around Dominica has not been investigated, we explore the first premise here. We note there is some doubt regarding the second premise based on a series of papers from the RICO experiment [see Krueger et al. (1997) and references therein]. These papers conclude, with reasonable certainty, that giant aerosol (e.g., sea salt) have no significant influence on the amount of precipitation produced by trade wind clouds.

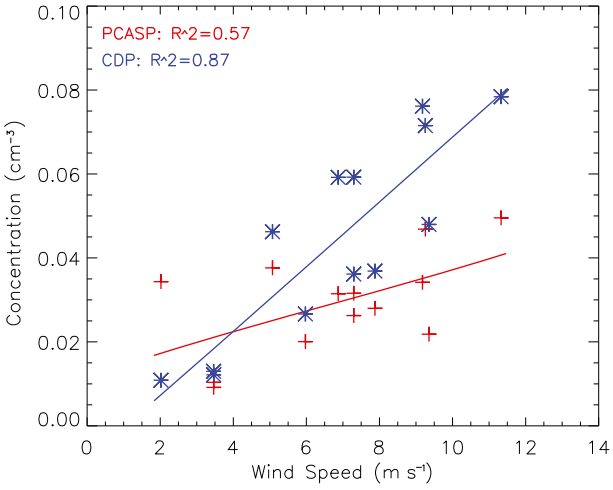

FIG. 13. Relationship between the ambient trade wind speed and the number concentration of giant aerosol/small droplets in the marine boundary layer at $z = 300$ m during 13 research flights when there was no large-scale cloudiness. The red plus signs show the giant aerosol concentration measured by PCASP (dried radius $> 0.5\,\mu$m), and the blue asterisks show the droplet concentration measured by CDP (radius $< 5\,\mu$m). All quantities, including trade wind speed, are the leg 1L average.

During DOMEX, the PCASP instrument was the primary measure of the aerosol size distribution (Cai et al. 2013). Along leg 1L, the PCASP captured an increase in the leg-average giant aerosol concentration as the trades strengthened (Fig. 13). However, the largest particle reliably detected by the PCASP has radius $1.5\,\mu$m, and the aircraft was not equipped with an instrument that could reliably detect larger aerosol. Sea-salt aerosols have been observed with radii larger than $5\,\mu$m (e.g., ultragiant aerosol), so two alternative measurements are hereby proposed.

The CDP uses a laser beam at the near-infrared wavelength ($\lambda = 0.658\,\mu$m) to detect scattering by liquid water droplets. Given sea-salt aerosol are strongly hygroscopic, and the marine boundary layer is humid (RH of 70%–90%), the sea salt probably exists as dissolved nuclei within small droplets (i.e., haze). Although the CDP measures droplet size rather than the size of the dry aerosol, it also shows a positive relationship between droplets of 1–5-μm radius and wind speed along leg 1L (Fig. 13).

The upward-pointing ultraviolet lidar ($\lambda = 0.355\,\mu$m) has measurements available at 3 Hz (every 20–30 m) and 3.75-m vertical range gates. Changes in backscattering intensity can provide valuable information about the droplet size as the light diffraction by each droplet ($<10\,\mu$m) would be in the Mie scattering regime and therefore proportional to the square of the droplet radius (Wang et al. 2009). A higher backscattering intensity may

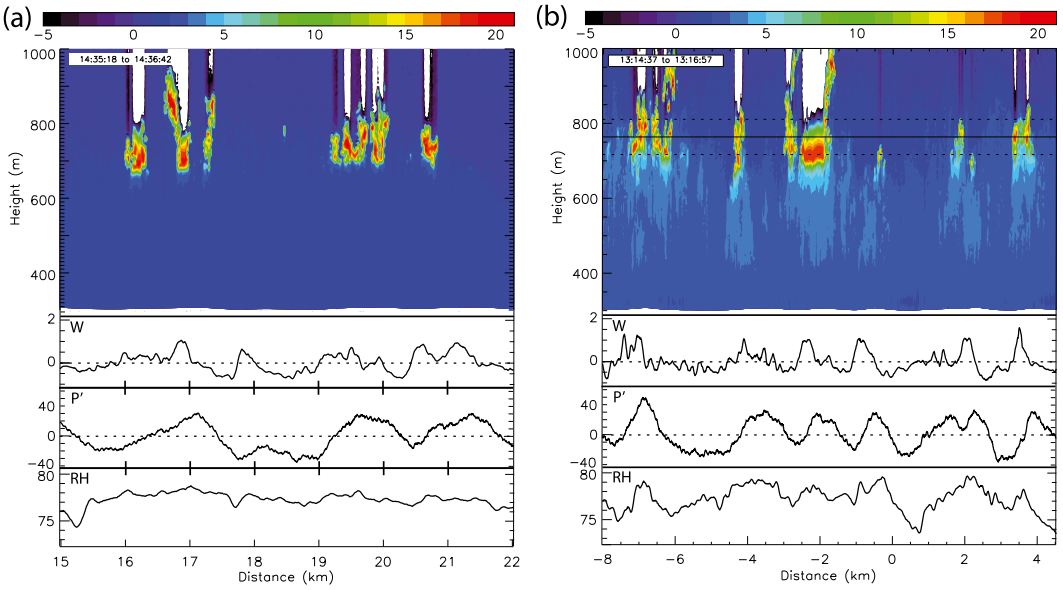

FIG. 14. A transect along leg 1L of (a) RF8 (low wind) and (b) RF12 (high wind) showing (top to bottom) the lidar backscattering intensity (dBZ), flight-level measurements at 300 m of vertical wind (w, m s^{-1}), pressure perturbation (P', Pa), and the relative humidity (RH, %). The flight-level measurements are at 1Hz (approximately every 80 m).

therefore indicate larger liquid droplets suspended in the marine boundary layer.

Figure 14 presents the backscattering intensity from the lidar along part of leg 1L for RF8 (low wind) and RF12 (high wind). Beneath each cloud during RF12 and other high wind days, an enhanced region of backscattering intensity extends approximately 300 m below cloud base. The upward-pointing cloud radar ($\lambda = 3.16$ mm with a minimum detectable signal of around -30 dBZ at 1 km) shows negligible backscattering in these "cloud roots," implying they are not drizzle from the cloud above. The cloud roots are most distinct on high wind days and are generally coincident with ascending air motion along leg 1L, a positive pressure perturbation, and elevated RH (Fig. 14b). Furthermore, the Doppler-shift winds derived from the cloud radar show upward motion at cloud base (not shown). We hypothesize that the cloud roots are regions of ascending motion, with the lidar capturing the hygroscopic growth, or deliquescence, of wetted sea salt rising toward cloud base.

To illustrate this, Fig. 15 presents the mean backscattering intensity beneath each cloud (averaged for each research flight) versus the estimated RH assuming a well-mixed and hydrostatic boundary layer and a relative humidity of 100% at cloud base (or distance beneath cloud base). The mean backscattering intensity is higher and increases more rapidly near cloud base as the trades strengthen, reminiscent of the increased droplet growth rate predicted by a Köhler curve (e.g., Fig. 1 in Manton 1983). The Köhler curve shows that larger and more hygroscopic aerosol are activated first near the cloud base, followed by progressively smaller and less hygroscopic aerosol as the supersaturation continues to increase. Given sea-salt aerosol are often giant and hygroscopic, their importance to this process is evident.

Finally, subcloud measurements during RF8 (the only low wind day when clouds were observed along leg 1L) suggest there is only a weak correlation between the flow field (especially w) at $z = 300$ m and the clouds aloft (Fig. 14a). This may be due to the smaller eddies in the boundary layer from the weaker trades. In contrast, on high wind days there is a relatively coherent pattern of moist updrafts beneath each cloud and weaker, drier

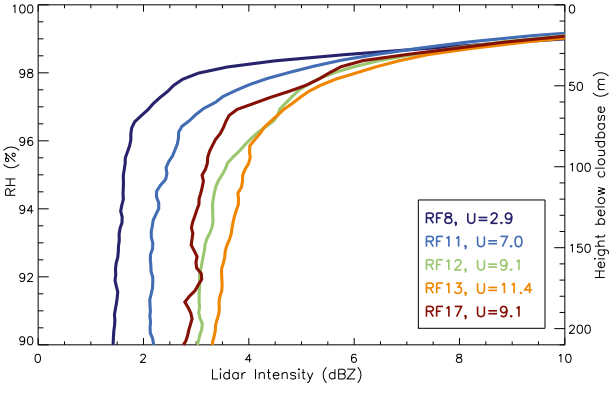

FIG. 15. The mean beneath-cloud lidar backscattering intensity vs estimated relative humidity (assuming hydrostatic equilibrium and 100% relative humidity at cloud base) along leg 1L. No clouds were observed aloft during RF7.

downdrafts elsewhere. The establishment of such a circulation may be important for the transport of surface-derived sea-salt aerosol into the growing cumulus clouds. On medium wind days, the correlation appears tighter although still not as strong compared to high wind days.

Observations during DOMEX strongly suggest sea-salt aerosol are present in the marine boundary layer upwind of Dominica on high wind days and that the sea salt enter the base of marine cumulus. While we make no attempt here to estimate the potential impact of this on the warm rain processes over Dominica, it forms a key component of our ongoing investigations. The RICO studies, which refute with some confidence that sea-salt aerosol can greatly enhance precipitation in marine cumulus, suggest the smaller island-derived aerosol are a controlling factor in precipitation over the island.

6. Summary and discussion

Observations from DOMEX showed that the shallow, orographic cumulus clouds forming over Dominica are quantitatively different from those over the open ocean. They are deeper, wider, and more closely packed; they have higher LWCs, stronger updrafts, and transport substantially more heat and water into the lower free troposphere; and they create a pronounced orographic enhancement of 3–5 times the over-ocean precipitation. However, DOMEX also revealed the orographic precipitation enhancement almost vanished when the trade winds weakened and over-island convection was driven by surface heating rather than forced ascent.

We proposed four hypotheses to explain this strong contrast in over-island precipitation, which relate to (i) the convection triggering mechanism, (ii) dry-air entrainment, (iii) giant sea-salt aerosol, and (iv) small island-derived aerosol. We have focused on the plausibility of the first three hypotheses. While all four hypotheses may exert some control on precipitation over Dominica, the competing processes make it difficult to determine the dominant mechanisms.

Aircraft observations showed the characteristics of the orographic cumulus clouds at flight level (z = 1.8 km) on low and high wind days were surprisingly similar, despite being triggered by different mechanisms. However, important differences emerged: on low wind days the orographic cumulus clouds were consistently shallower than on high wind days, with larger cloud droplet number densities and smaller MVDs.

The shallower clouds were likely caused by the drier cloud-layer and lower trade wind inversion observed upwind of Dominica on the two low wind days. We used a simple entraining parcel model and the WRF Model (with a heat bubble in the boundary layer to trigger convection) to qualitatively demonstrate that cloud-layer moisture variations can control cumulus depth and LWC through dry-air entrainment. Cloud size also plays an important role—wider clouds protect the interior core region from entrained air—however, there is no evidence that the orographic cumulus on high wind days are consistently wider than on low wind days.

While the model simulations were useful in some qualitative ways, their interpretations were partly undermined by our inability to constrain α_E in the parcel model and K in the WRF Model. Cumulus development was surprisingly sensitive to these entrainment-related parameters—especially K, which is meant to represent the background turbulence and mixing. In addition, quantifying how the diurnal–thermal convection modified the above-island environment throughout the day without further observations remains an outstanding issue. The reverse westerly flow above the trade wind inversion may also impact cumulus development, possibly detaching the cloud tops from the cloud bases (C. C. Wang and D. J. Kirshbaum 2014, personal communication).

A further concern is the representativeness of the DOMEX observations in April–May 2011. A 5-week project is probably not sufficiently long to give statistically robust results. We analyzed 14 yr of soundings from the neighboring island of Guadeloupe and found the dry conditions observed on the two low wind days are, while relatively infrequent, more often associated with weaker trade winds. Perhaps surprisingly, the low wind days during DOMEX, which were considered dry with respect to conditions observed during the field project, were more moist than what could be considered ''dry'' conditions based on the Guadeloupe soundings. The impact of an even drier and shallower cloud layer on the orographic cumulus warrants further study.

Finally, the different cloud droplet spectrum during thermal and mechanical convection may be related to either the third or fourth hypothesis (or both). Smith et al. (2012) suggests that island-derived aerosol are responsible for the higher cloud droplet number density and smaller MVD, although observations upwind of Dominica seem to show deliquescing sea-salt aerosol entering the base of marine cumulus when the trades were strong. A parallel investigation using the WRF Model with a more sophisticated microphysics scheme shows island-derived aerosol finding their way into the cloud system and reducing the cloud droplet MVD in low wind, thermally driven conditions (A. D. Nugent 2014, personal communication). However, existing models are still unable to simulate different aerosol sources and properties simultaneously. Until this is addressed, it will be difficult to determine the role of

aerosol in cloud microphysics over Dominica without additional observations.

Acknowledgments. The authors would like to thank Jeffrey French for help with the DOMEX observations; Daniel Kirshbaum, Chun-Chih Wang, Justin Minder, and Jorgen Jensen for useful conversations; and the Yale High Performance Computing Center for access to their facilities. This work was funded by NSF Grant 0930356.

APPENDIX A

Idealized Soundings

Three idealized soundings are used to initialize WRF: Moist, Dry, and Dry_{MOD} (Fig. 10). The Moist is based on the observed upwind profiles from the three high wind days [RF12, RF13, and RF17; Minder et al. (2013) and Nugent et al. (2014) used a similar sounding in their studies].

The Dry is based on the observed upwind profiles from the two low wind days (RF7 and RF8). The temperature profile is adjusted to ensure T_v is identical to Moist at all levels, motivated by observed similarities in dT_v/dz in the upwind profiles on low and high wind days (Fig. 7b). When adjusted, Dry has a neutral temperature lapse rate immediately above the mixed layer, consistent with observations.

The Dry_{MOD} represents how the environment above Dominica may be modified by the thermally driven convection based on the leg-average out-of-cloud mixing ratio along LOW-4. The temperature profile is also adjusted to ensure T_v is identical to Moist at all levels.

Below $z = 700$ m, all soundings are identical to each other. Above the height of the observations ($z = 4$ km), all soundings relax to that used in the BOMEX model experiments (Siebesma et al. 2003).

APPENDIX B

The WRF Model

The WRF Model domain is 30 km × 30 km in the x and y direction with a horizontal grid spacing of 50 m. There are 152 vertical levels with a vertical grid spacing of around 50 m in the lowest 4 km and a model top at 12 km. The lateral boundaries are periodic and a Rayleigh damping layer is used above 8 km. The bottom boundary conditions have no surface or moisture fluxes, and surface friction and rotation is neglected. There is also no representation of atmospheric radiative fluxes, large-scale subsidence, or environmental winds.

Cloud and precipitation microphysics are parameterized using the Kessler warm-rain scheme (Kessler 1969). The cloud is initiated with a single, Gaussian-shaped heat bubble at the start of the model simulation, located within the boundary layer in the middle of the domain. The heat bubble has a vertical radius of 375 m; a horizontal radii of $R_B = 375$ m, 750 m, and 1.5 km (equidistant in the x and y direction); and a maximum temperature perturbation of 1°C at its center. This is larger than the hypothesized 0.2°C perturbation generated when subcloud humidity fluctuations are lifted by the terrain (Nugent and Smith 2014), which was found to be insufficient to initiate cloud in these idealized environments.

Motivated by the results of Carpenter et al. (1998), who found a turbulent boundary layer is required for sufficient entrainment to occur into shallow cumulus, we performed additional heat bubble simulations with prognostic TKE and specified background turbulence (following Blyth et al. 2005). While this allowed for more realistic cumulus development and cloud adiabatic fractions, the sensitivity of the maximum cloud-top height and LWC to variations in R_B was similar to simulations where the background turbulence was accounted for with a prescribed eddy diffusivity rate (i.e., K).

REFERENCES

Abel, S. J., and B. J. Shipway, 2007: A comparison of cloud-resolving model simulations of trade wind cumulus with aircraft observations taken during RICO. *Quart. J. Roy. Meteor. Soc.,* **133,** 781–794, doi:10.1002/qj.55.

Arakawa, A., and W. Schubert, 1974: Interaction of a cumulus cloud ensemble with the large-scale environment. *J. Atmos. Sci.,* **31,** 674–701, doi:10.1175/1520-0469(1974)031<0674:IOACCE>2.0.CO;2.

Aspliden, C. I., 1976: A classification of the structure of the tropical atmosphere and related energy fluxes. *J. Appl. Meteor.,* **15,** 692–697, doi:10.1175/1520-0450(1976)015<0692:ACOTSO>2.0.CO;2.

Austin, J., 1948: A note on cumulus growth in a nonsaturated environment. *J. Meteor.,* **5,** 103–107, doi:10.1175/1520-0469(1948)005<0103:ANOCGI>2.0.CO;2.

Batchelor, G. K., 1967: *An Introduction to Fluid Mechanics.* Cambridge University Press, 615 pp.

Betts, A., and W. Ridgway, 1989: Climatic equilibrium of the atmospheric convective boundary layer over a tropical ocean. *J. Atmos. Sci.,* **46,** 2621–2641, doi:10.1175/1520-0469(1989)046<2621:CEOTAC>2.0.CO;2.

Blyth, A. M., W. A. Cooper, and J. B. Jensen, 1988: A study of the source of entrained air in Montana cumuli. *J. Atmos. Sci.,* **45,** 3944–3964, doi:10.1175/1520-0469(1988)045<3944:ASOTSO>2.0.CO;2.

——, S. G. Lasher-Trapp, and W. A. Cooper, 2005: A study of thermals in cumulus clouds. *Quart. J. Roy. Meteor. Soc.,* **131,** 1171–1190, doi:10.1256/qj.03.180.

——, J. H. Lowenstein, Y. Huang, Z. Cui, S. Davies, and K. S. Carslaw, 2013: The production of warm rain in shallow maritime cumulus clouds. *Quart. J. Roy. Meteor. Soc.,* **139,** 20–31, doi:10.1002/qj.1972.

Bryan, G. H., J. C. Wyngaard, and J. M. Fritsch, 2003: Resolution requirements for the simulation of deep moist convection. *Mon. Wea. Rev.,* **131,** 2394–2416, doi:10.1175/1520-0493(2003)131<2394:RRFTSO>2.0.CO;2.

Cai, Y., J. R. Snider, and P. Wechsler, 2013: Calibration of the passive cavity aerosol spectrometer probe for airborne determination of the size distribution. *Atmos. Meas. Tech.,* **6,** 2349–2358, doi:10.5194/amt-6-2349-2013.

Carpenter, R. L., K. K. Droegemeier, and A. M. Blyth, 1998: Entrainment and detrainment in numerically simulated cumulus congestus clouds. Part I: General results. *J. Atmos. Sci.,* **55,** 3417–3432, doi:10.1175/1520-0469(1998)055<3417:EADINS>2.0.CO;2.

Cooper, W. A., R. T. Bruintjes, and G. K. Mather, 1997: Calculations pertaining to hygroscopic seeding with flares. *J. Appl. Meteor.,* **36,** 1449–1469, doi:10.1175/1520-0450(1997)036<1449:CPTHSW>2.0.CO;2.

Davison, J. L., R. M. Rauber, L. Di Girolamo, and M. A. LeMone, 2013a: A revised conceptual model of the tropical marine boundary layer. Part I: Statistical characterization of the variability inherent in the wintertime trade wind regime over the western tropical Atlantic. *J. Atmos. Sci.,* **70,** 3005–3024, doi:10.1175/JAS-D-12-0321.1.

——, ——, ——, and ——, 2013b: A revised conceptual model of the tropical marine boundary layer. Part II: Detecting relative humidity layers using Bragg scattering from S-band radar. *J. Atmos. Sci.,* **70,** 3025–3046, doi:10.1175/JAS-D-12-0322.1.

——, ——, ——, and ——, 2013c: A revised conceptual model of the tropical marine boundary layer. Part III: Bragg scattering layer statistical properties. *J. Atmos. Sci.,* **70,** 3047–3062, doi:10.1175/JAS-D-12-0323.1.

de Rooy, W. C., and Coauthors, 2013: Entrainment and detrainment in cumulus convection: An overview. *Quart. J. Roy. Meteor. Soc.,* **139,** 1–19, doi:10.1002/qj.1959.

Eastin, M. D., P. G. Black, and W. M. Gray, 2002: Flight-level thermodynamic instrument wetting errors in hurricanes. Part I: Observations. *Mon. Wea. Rev.,* **130,** 825–841, doi:10.1175/1520-0493(2002)130<0825:FLTIWE>2.0.CO;2.

Heus, T., and H. J. J. Jonker, 2008: Subsiding shells around shallow cumulus clouds. *J. Atmos. Sci.,* **65,** 1003–1018, doi:10.1175/2007JAS2322.1.

Jensen, J. B., and S. Lee, 2008: Giant sea-salt aerosols and warm rain formation in marine stratocumulus. *J. Atmos. Sci.,* **65,** 3678–3694, doi:10.1175/2008JAS2617.1.

——, P. H. Austin, M. B. Baker, and A. M. Blyth, 1985: Turbulent mixing, spectral evolution and dynamics in a warm cumulus cloud. *J. Atmos. Sci.,* **42,** 173–192, doi:10.1175/1520-0469(1985)042<0173:TMSEAD>2.0.CO;2.

Johnson, D. B., 1982: The role of giant and ultragiant nuclei in warm rain initiation. *J. Atmos. Sci.,* **39,** 448–460, doi:10.1175/1520-0469(1982)039<0448:TROGAU>2.0.CO;2.

Kessler, E., 1969: *On the Distribution and Continuity of Water Substance in Atmospheric Circulation. Meteor. Monogr.,* No. 32, Amer. Meteor. Soc., 84 pp.

Kirshbaum, D. J., 2013: On thermally forced circulations over heated terrain. *J. Atmos. Sci.,* **70,** 1690–1709, doi:10.1175/JAS-D-12-0199.1.

——, and R. B. Smith, 2009: Orographic precipitation in the tropics: Large-eddy simulations and theory. *J. Atmos. Sci.,* **66,** 2559–2578, doi:10.1175/2009JAS2990.1.

——, and A. L. M. Grant, 2012: Invigoration of cumulus cloud fields by mesoscale ascent. *Quart. J. Roy. Meteor. Soc.,* **138,** 2136–2150, doi:10.1002/qj.1954.

Krueger, S. K., C.-W. Su, and P. A. McMurty, 1997: Modeling entrainment and finescale mixing in cumulus clouds. *J. Atmos. Sci.,* **54,** 2697–2712, doi:10.1175/1520-0469(1997)054<2697:MEAFMI>2.0.CO;2.

Lance, S., C. A. Brock, D. Rogers, and J. A. Gordon, 2010: Water droplet calibration of the Cloud Droplet Probe (CDP) and in-flight performance in liquid, ice and mixed-phase clouds during ARCPAC. *Atmos. Meas. Tech.,* **3,** 1683–1706, doi:10.5194/amt-3-1683-2010.

Manton, M. J., 1983: The physics of clouds in the atmosphere. *Rep. Prog. Phys.,* **46,** 1393–1444, doi:10.1088/0034-4885/46/12/001.

Minder, J. R., R. B. Smith, and A. D. Nugent, 2013: The dynamics of ascent-forced orographic convection in the tropics: Results from Dominica. *J. Atmos. Sci.,* **70,** 4067–4088, doi:10.1175/JAS-D-13-016.1.

Morton, B. R., G. Taylor, and J. S. Turner, 1956: Turbulent gravitational convection from maintained and instantaneous sources. *Proc. Roy. Soc. London,* **234A,** 1–23, doi:10.1098/rspa.1956.0011.

Neggers, R. A. J., A. P. Siebesma, and H. J. J. Jonker, 2002: A multiparcel model for shallow cumulus convection. *J. Atmos. Sci.,* **59,** 1655–1668, doi:10.1175/1520-0469(2002)059<1655:AMMFSC>2.0.CO;2.

Nie, J., and Z. Kuang, 2012: Responses of shallow cumulus convection to large-scale temperature and moisture perturbations: A comparison of large-eddy simulations and a convective parameterization based on stochastically entraining parcels. *J. Atmos. Sci.,* **69,** 1936–1956, doi:10.1175/JAS-D-11-0279.1.

Nugent, A. D., and R. B. Smith, 2014: Initiating moist convection in an inhomogeneous layer by uniform ascent. *J. Atmos. Sci.,* **71,** 4597–4610, doi:10.1175/JAS-D-14-0089.1.

——, ——, and J. R. Minder, 2014: Wind speed control on tropical orographic convection. *J. Atmos. Sci.,* **71,** 2695–2712, doi:10.1175/JAS-D-13-0399.1.

Nuijens, L., and B. Stevens, 2012: The influence of wind speed on shallow marine cumulus convection. *J. Atmos. Sci.,* **69,** 168–184, doi:10.1175/JAS-D-11-02.1.

——, ——, and A. P. Siebesma, 2009: The environment of precipitating shallow cumulus convection. *J. Atmos. Sci.,* **66,** 1962–1979, doi:10.1175/2008JAS2841.1.

Rauber, R. M., and Coauthors, 2007: Rain in Shallow Cumulus over the Ocean: The RICO campaign. *Bull. Amer. Meteor. Soc.,* **88,** 1912–1928, doi:10.1175/BAMS-88-12-1912.

Romps, D. M., and Z. Kuang, 2010: Nature versus nurture in shallow convection. *J. Atmos. Sci.,* **67,** 1655–1666, doi:10.1175/2009JAS3307.1.

Russotto, R. D., T. Storelvmo, and R. B. Smith, 2013: Modeling aerosol activation in a tropical, orographic, island setting: Sensitivity tests and comparison with observations. *Atmos. Res.,* **134,** 12–23, doi:10.1016/j.atmosres.2013.07.017.

Sherwood, S. C., D. Hernandez-Deckers, and M. Colin, 2013: Slippery thermals and the cumulus entrainment paradox. *J. Atmos. Sci.,* **70,** 2426–2442, doi:10.1175/JAS-D-12-0220.1.

Siebesma, A. P., and Coauthors, 2003: A large eddy simulation intercomparison study of shallow cumulus convection. *J. Atmos. Sci.,* **60,** 1201–1219, doi:10.1175/1520-0469(2003)60<1201:ALESIS>2.0.CO;2.

Skamarock, W. C., and Coauthors, 2008: A description of the Advanced Research WRF version 3. NCAR Tech. Note. NCAR/TN-475+STR, 113 pp. [Available online at http://www.mmm.ucar.edu/wrf/users/docs/arw_v3_bw.pdf.]

Smith, R. B., P. Schafer, D. J. Kirshbaum, and E. Regina, 2009: Orographic precipitation in the tropics: Experiments in Dominica. *J. Atmos. Sci.,* **66,** 1698–1716, doi:10.1175/2008JAS2920.1.

——, and Coauthors, 2012: Orographic precipitation in the tropics: The Dominica experiment. *Bull. Amer. Meteor. Soc.,* **93,** 1567–1579, doi:10.1175/BAMS-D-11-00194.1.

Stevens, B., and J.-L. Brenguier, 2009: Cloud-controlling factors. *Clouds in the Perturbed Climate System,* J. Heintzenberg and R. Charlson, Eds., MIT Press, 173–196.

Wang, Y., and B. Geerts, 2009: Estimating the evaporative cooling bias of an airborne reverse flow thermometer. *J. Atmos. Oceanic Technol.,* **26,** 3–21, doi:10.1175/2008JTECHA1127.1.

Wang, Z., P. Wechsler, W. Kuestner, J. French, A. Rodi, B. Glover, M. Burkhart, and D. Lukens, 2009: Wyoming Cloud Lidar: Instrument description and applications. *Opt. Express,* **17,** 13 576–13 587, doi:10.1364/OE.17.013576.

Warner, J., 1970: On steady-state one-dimensional models of cumulus convection. *J. Atmos. Sci.,* **27,** 1035–1040, doi:10.1175/1520-0469(1970)027<1035:OSSODM>2.0.CO;2.

Woodcock, A. H., 1953: Salt nuclei in marine air as a function of altitude and wind force. *J. Meteor.,* **10,** 362–371, doi:10.1175/1520-0469(1953)010<0366:SNIMAA>2.0.CO;2.

——, 1960: The origin of trade-wind orographic shower rains. *Tellus,* **12,** 315–326, doi:10.1111/j.2153-3490.1960.tb01316.x.

Zehnder, J. A., J. Hu, and A. Radzan, 2009: Evolution of the vertical thermodynamic profile during the transition from shallow to deep convection during CuPIDO 2006. *Mon. Wea. Rev.,* **137,** 937–953, doi:10.1175/2008MWR2829.1.

Zhao, M., and P. H. Austin, 2005: Life cycle of numerically simulated shallow cumulus clouds. Part II: Mixing dynamics. *J. Atmos. Sci.,* **62,** 1291–1310, doi:10.1175/JAS3415.1.